Universidade de São Paulo
Instituto de Física

Transições topológicas em escadas de Kane-Mele-Hubbard

Rafael Miksian Magaldi

Orientador: Prof. Dr. Luis Gregório G. V. Dias da Silva

Dissertação de mestrado apresentada ao Instituto de Física da Universidade de São Paulo, como requisito parcial para a obtenção do título de Mestre(a) em Ciências.

Banca Examinadora:
Prof. Dr. Luis Gregório G. V. Dias da Silva - IFUSP
Prof. Dr. Eric de Castro e Andrade - IFSC/USP
Profa. Dra. Maria Carolina de Oliveira Aguiar - UFMG

São Paulo
2019

University of São Paulo
Physics Institute

Topological transitions in Kane-Mele-Hubbard ladders

Rafael Miksian Magaldi

Supervisor: Prof. Dr. Luis Gregório G. V. Dias da Silva

Dissertation submitted to the Physics Institute of the
University of São Paulo in partial fulfillment of the
requirements for the degree of Master of Science.

Examining Committee:
Prof. Dr. Luis Gregório G. V. Dias da Silva - IFUSP
Prof. Dr. Eric de Castro e Andrade - IFSC/USP
Profa. Dra. Maria Carolina de Oliveira Aguiar - UFMG

São Paulo
2019

To my family.

Acknowledgments

Conducting this project was a truly enriching journey. It allowed me to learn a great deal about both topology in condensed matter and tensor networks algorithms applied to physics, themes which I intend to study further in my future career. It also helped me develop valuable skills necessary to independent research, such as coding, writing and presenting my work. None of this would be possible without the help of many people, some of whom I would like to thank here.

To my advisor Prof. Dr. Luis Gregório Dias da Silva, I thank you for introducing me to this project and helping me develop it throughout these years. I am grateful for all you taught me regarding condensed matter and computation.

To my family, I thank you all for supporting me in my dream of becoming a researcher. You made everything easy for me, and I am eternally grateful for that.

To the friends I made during my time at USP, thank you for helping me an uncountable amount of times both with the courses we took and with the development of this project. Your camaraderie was invaluable and I will always remember you all kindly.

To the ever-patient Manoela Reis, thank you for always believing in me.

I would also like to thank CNPq for the financial support during this project.

This research project was developed with the aid of high performance computing resources made available from the Superintendence of Information Technology of the University of São Paulo.

”I shall be telling this with a sigh
Somewhere ages and ages hence:
Two roads diverged in a wood, and I—
I took the one less traveled by,
And that has made all the difference.”
- Robert Frost

Abstract

Topological insulators are materials that behave as insulators in the bulk, but present conducting edge states. Despite the growing interest in such materials due to their possible applications on spintronic devices and quantum computing, several open questions still remain regarding the roles of both electronic interactions and dimensionality in these systems.

The goal of this work is to tackle some of these questions. To do so, we study a quasi-1D system presenting a topologically non-trivial phase and electronic interactions: the so-called Kane-Mele-Hubbard ladders. Here, we apply the density matrix renormalization group (DMRG) algorithm in the tensor network formalism in order to calculate some physical properties of this system. The DMRG calculations allow us to reach the system's ground state and enable the efficient computation of observables and of the entanglement entropy.

The Kane-Mele-Hubbard model is an interacting version of the Kane-Mele model, which displays topologically non-trivial phases. The interest on this system is due to the combination of effects caused by the spin-orbit coupling and the electronic interactions. For the non-interacting case we have a topological insulator, whereas in the highly interacting picture we have a Mott insulator with localized electrons.

We explore the phase transition between these regimes, looking at the conditions needed for the appearance of spin-polarized edge states. We also propose the entanglement entropy between two halves of the system as an indicator of the topological phase transition, as it presents a particular pattern when the phase transition takes place.

Keywords: Topological insulators; Electronic interactions; Kane-Mele-Hubbard; Tensor networks; Density matrix renormalization group.

Resumo

Isolantes topológicos são materiais que se comportam como isolantes no “bulk”, mas apresentam estados condutores nas bordas. Apesar do crescente interesse nesses materiais devido a suas possíveis aplicações em dispositivos de spintrônica e computação quântica, ainda restam diversas questões em aberto sobre a influência tanto de interações eletrônicas como da dimensionalidade nesses sistemas.

O objetivo desse trabalho é abordar algumas dessas questões. Para tal, estudamos um sistema quasi-1D contendo uma fase topológica não-trivial e interações eletrônicas: as chamadas escadas de Kane-Mele-Hubbard. Aqui, aplicamos o algoritmo do grupo de renormalização da matriz de densidade (DMRG) com o formalismo de redes de tensores para calcular algumas propriedades físicas desse sistema. Os cálculos de DMRG permitem acessar o estado fundamental do sistema e proporcionam a computação eficiente de observáveis e da entropia de emaranhamento.

O modelo de Kane-Mele-Hubbard é uma versão interagente do modelo de Kane-Mele, o qual apresenta fases topológicas não-triviais. O interesse nesse sistema se dá pela combinação de efeitos causados pelo acoplamento spin-órbita e pela interação eletrônica. Para o caso não-interagente, temos um isolante topológico, enquanto que no caso altamente interagente temos um isolante de Mott com elétrons localizados.

Exploramos a transição de fase entre esses dois regimes, observando as condições necessárias para o surgimento de estados de borda spin polarizados. Também propomos a entropia de emaranhamento entre as duas metades do sistema como um indicador da transição de fase topológica, uma vez que ela apresenta um padrão particular quando ocorre a transição.

Palavras-chave: Isolantes topológicos; Interações eletrônicas; Kane-Mele-Hubbard; Rede de tensores; Grupo de renormalização da matriz de densidade.

Contents

1 Introduction 17

1.1 Topological Phases of Matter 18

1.2 DMRG and Tensor Networks 19

1.3 Dissertation Outline 20

2 Topological phases in Condensed Matter systems 22

2.1 Topological Insulators 22

2.2 From QHE to the Kane-Mele model 23

2.2.1 Haldane model 24

2.2.2 Kane-Mele model 26

2.3 Electronic interactions and the Kane-Mele-Hubbard model 28

3 DMRG and the tensor network matrix product state formalism 32

3.1 Density matrix renormalization group algorithm 33

3.1.1 Motivation: truncated diagonalization 33

3.1.2 Truncation based on proximity to ground state 35

3.1.3 Density matrices 36

3.1.4 Singular value decomposition and Schmidt decomposition . . . 37

3.1.5 Infinite-size DMRG 39

3.1.6 Finite-size DMRG 40

3.2 Matrix product states as tensor networks 41
3.3 Measuring observables 45
3.3.1 Singular value decomposition and MPS gauge 46
3.3.2 Truncating the MPS 50
3.4 DMRG with tensor networks 51
3.4.1 Matrix product operators 52
3.4.2 DMRG in the TN/MPS formulation 53
3.5 Calculating the entanglement entropy 55
3.5.1 Entanglement 55
3.5.2 The von Neumann entropy 56

4 Kane-Mele-Hubbard ladders 58
4.1 Representing Kane-Mele-Hubbard ladders in 1D 58
4.2 Ground state energy finite size scaling 60
4.3 Spin polarization 64
4.4 Entanglement entropy 67

5 Conclusions 73

Appendix A Kane-Mele model tight-binding Hamiltonian 78

Annexes 83

I Best Poster Award at the Brazilian Physical Society Autumn Meeting 84

List of Figures

1.1 Kane-Mele-Hubbard ladder. 19

2.1 Figure from [15]. Representation of topological phase transitions of closed 2-dimensional surfaces in 3 dimensions. 23

2.2 Figure from [17]. The Haldane model. Dots with different colors (black or white) are from different sublattices, with different on-site energies. Areas a have magnetic flux ϕ, whereas areas b have magnetic flux $-\phi$ and area c has no magnetic flux. This way, the net flux through the unit cell is zero. 24

2.3 Figure from [17]. Phase diagram of the Haldane model. 25

2.4 Figure from [10]. Energy bands for 1D strip. In both cases we have $\lambda_{SO} = 0.06t$ and $\lambda_R = 0.05t$, but (a) shows the QSHE phase with $\lambda_\nu = 0.1t$, while (b) shows a trivial insulator with $\lambda_\nu = 0.5t$. The inset shows a phase diagram for $0 < \lambda_{SO} \ll t$. 27

2.5 Edited figure from [26]. Simplified Kane-Mele model with tight-binding and spin-orbit interactions only. The arrows show the positive direction $+i\lambda_{SO}$ from the sign of $\hat{e}_{\mathbf{i},\mathbf{k}} \cdot \sigma$. 29

2.6 Figure from [11]. Phase diagram of the 2D Kane-Mele-Hubbard model, presenting the Semi-Metal (SM), Quantum Spin Hall Insulator (QSHI) and Antiferromagnetic Insulator (AFMI) phases. 30

3.1 Figure from [27]. Depiction of the block-growth process in the infinite-size DMRG. Starting from the blocks on step (**a**), we add a new site to each block (**b**), obtain the ground state of the whole system (**c**) and calculate the reduced density matrices to rotate the system to the new basis keeping only the m largest eigenvalues of the density matrices, generating a new block (**d**) for the next iteration. 40
3.2 Figure from [27]. Depiction of the sweeps in the finite-size DMRG algorithm. Starting from the blocks from the infinite-size DMRG, we conduct sweeps from one direction to the other and vice versa, in a way that as one block grows, the other shrinks. 41
3.3 Figure from [28]. 5-site MPS and its representation as a TN. 42
3.4 Figure from [28]. Contraction of two tensors in a TN. 43
3.5 Figure from [28]. 10-site wave function as only one tensor. 43
3.6 Figure from [28]. Norm of the 10-site wave function. 43
3.7 Figure from [28]. Calculating the norm of Ψ with MPS. 44
3.8 Figure from [28]. Indexes' dimensions for calculation of MPS contractions cost. We can see both types of contractions have the same cost of m^3d. 45
3.9 Figure from [28]. Expectation value of operator A acting on sites 3 and 4 of a chain. 45
3.10 Figure from [28]. Contracting tensors from sites outside of the measurement makes the calculation more efficient, just like when calculating the norm. 46
3.11 Figure from [28]. SVD applied to a wave function and its TN graphical representation. 47
3.12 Figure from [28]. SVD of two-site wave function and its TN graphical representation as an MPS. 47

3.13 Figure from [28]. Iteratively applying SVDs to an MPS will create a chain of unitary tensors. 48
3.14 Figure from [28]. MPS can be adjusted (gauged) via SVDs so that the tensor with singular values can stay at any position in the chain. 48
3.15 Figure from [28]. Orthogonality of U and V in the TN representation. . 49
3.16 Figure from [28]. Using the orthogonality of U and V and the proper gauge of the MPS, the expectation value calculation is much simpler. . . 49
3.17 Figure from [28]. Graphical representation of an MPO. 52
3.18 Figure from [28]. Steps of the DMRG algorithm implemented via TN/MPS. 55
3.19 Figure from [28]. TN representation of the reduced density matrix. It is obtained after taking the partial trace over one partition of the system. . 56

4.1 Kane-Mele-Hubbard ladders in (a) hexagonal chain and topologically equivalent forms of (b) stair and (c) linear chain, this last one proper to the DMRG algorithm. 59
4.2 Finite-size scaling of the energy of the ground state, using chains of 22 to 90 sites, and parameters $t = 1$, $\lambda_{SO} = 0.5$, $U = 5$. 61
4.3 Finite-size scaling for the ground state energy with $t = 1$, $\lambda_{SO} = 0$ and varying U. 62
4.4 Finite-size scaling for the ground state energy with $t = 1$, $\lambda_{SO} = 0.25$ and varying U. 62
4.5 Finite-size scaling for the ground state energy with $t = 1$, $\lambda_{SO} = 0.5$ and varying U. 63
4.6 Finite-size scaling for the ground state energy with $t = 1$, $\lambda_{SO} = 1$ and varying U. 63
4.7 Contour plot of the ground state energy extrapolated to the thermodynamic limit as a function of λ_{SO} and U. 64

4.8 Color code for the 4 different types of sites in the chain, along with the numbering used for the sites. 65
4.9 Spin polarization in all the 90 sites of the chain as λ increases. 66
4.10 Spin polarization in the chain. The increase in U caused the disappearance of polarized states. 67
4.11 Entanglement entropy between the halves of the system as a function of λ. 68
4.12 Zoom into the entanglement entropy (in the region of the phase transition), as a function of λ and for different values of U, for $N = 90$ sites. 69
4.13 Figure from [34]. The three-leg spin tube model. 70
4.14 Figure from [34]. Entanglement entropy in the 1D bilinear-biquadractic model as a function of its tunable parameter θ. S^H (S^I) represents the system with half-integer (integer) spin representation on the ends of the chain. The dashed and full lines represent different sizes $L = 200, 500$ of the chain. All entanglement entropy curves present a sudden increase in the region of the topological phase transition, in the proximity of the vertical red dashed line. 71
4.15 Figure from [34]. Entanglement entropy in the quasi-1D three-leg spin tube model as a function of its tunable parameter α. S^H (S^I) represents the system with half-integer (integer) spin representation on the ends of the chain. Both curves present a sudden increase in the region of the topological phase transition. 71

A.1 Hexagonal chain with vector basis. 79

Chapter 1

Introduction

In this work, we study the influence of electronic interactions in the properties of a system with topologically non-trivial phases. These interactions are commonly neglected when developing theoretical models to study topological phases arising from the interplay of spin-orbit interaction and time-reversal symmetry in the band structure of some topological materials, as non-interacting models can describe their properties fairly well. This is the case for topological insulators such as 2-dimensional HgTe/CdTe wells [1] and some 3-dimensional crystals (Bi_2Te_3 and Bi_2Se_3 [2], for instance). However, there has been a growing interest in the study of the connection between correlation effects and topological phases, as their combined effects might be responsible for exotic behavior, such as spin liquid phases in topological insulators [3] [4], topological Mott insulators [5] and topological Kondo insulators [6].

The model analyzed here is described by the Kane-Mele-Hubbard Hamiltonian [7] [8], which includes tight-binding, spin-orbit and on-site Hubbard interactions in a honeycomb chain. The interest in this system is based on the combination of effects caused by spin-orbit coupling and electronic interactions. In the absence of such interactions, the model describes a topological insulator characterized by a Z_2 invariant [10]. On the other hand, in the highly-interacting limit, the system behaves as a Mott insulator with quasi-long range antiferromagnetic ordering. When spin-orbit coupling and Coulombic repulsion are of the same order of magnitude, the behaviour of the system becomes more interesting, with a phase transition between the two regimes [11].

One of the reasons for the difficulty in studying this phase transition is how challenging it is to treat interacting many-body systems. Since the Hamiltonian is not solvable analytically, it becomes necessary to resort to numerical methods to approach the problem. Here, we choose the tensor network framework, taking use of the ITensor library [9], because tensor networks are a great tool to describe many-body systems [12] [13] [14].

In the following subsections, we introduce some of the physical themes relevant to this work, as well as the basic ideas of the numerical methods used. A more detailed view of those topics is presented in the next chapters.

1.1 Topological Phases of Matter

In recent years, there has been an increasing interest by the condensed matter community on the role of topology in the properties of electronic systems. The 2016 Nobel prize exemplifies this, as it was awarded to J. Michael Kosterlitz, F. Duncan Haldane and David J. Thouless for their important work on the field of topological phases of matter and topological transitions [15].

This topic was first brought to light in the 1980's with the discovery of the Quantum Hall Effect (QHE) by Klaus von Klitzing [16]. Systems that present QHE behave as an insulator in the bulk while presenting conducting edge states. This means these systems cannot be characterized by a local order parameter, indicating a rupture from Landau's paradigm [17]. In fact, a non-local topological order parameter is used to describe their phases, which led to the nomenclature of "topological insulators".

Later, Charles Kane and Eugene Mele, while studying the effects of spin-orbit interactions, proposed graphene as a candidate for a 2D topological insulator [10] [18]. This led to a great resurgence of the theme. Even though the topological phase transition was never observed in graphene due to its low spin-orbit coupling, it was soon after theoretically predicted [19] and experimentally observed [20] in HgTe quantum wells.

Since then, many efforts were conducted at the search of new systems presenting topologically non-trivial phases. However, for the most part, they were focused only on two-dimensional non-interacting systems. Therefore, several questions remain regarding the effects of both electronic interactions and dimensionality on these systems. In this work, we will try to tackle these questions, as we study a topological phase transition on a quasi-1D structure presenting electronic interactions: the Kane-Mele-Hubbard ladders, as shown in Figure 1.1. The Kane-Mele-Hubbard Hamiltonian is based on the Kane-Mele model [10][18], from where it borrows a first-neighbor hopping term and a second-neighbor spin-orbit coupling term. Then, we just add the Hubbard interactions in each site of the chain, representing the Coulombic repulsion between electrons in the same site, to create this interacting model [7] [8].

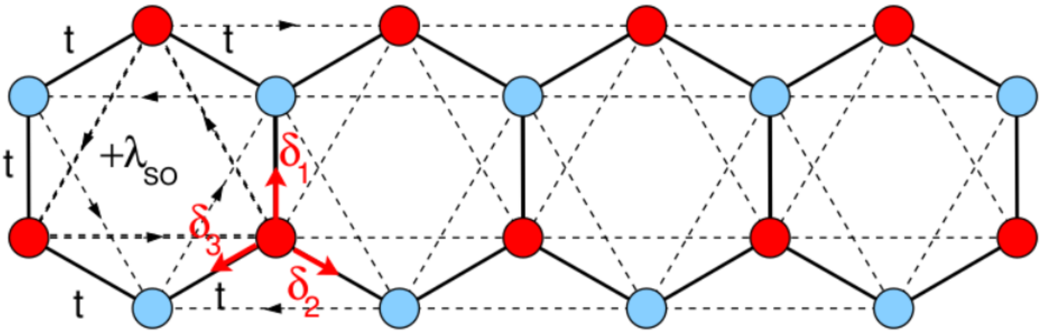

Figure 1.1: Kane-Mele-Hubbard ladder.

1.2 DMRG and Tensor Networks

In this section, we will present a brief overview of the numerical methods we applied in this work. A more in-depth discussion will be conducted in chapter 3.

In 1992, Steven White created a revolutionary algorithm to study quantum many-body systems: the density matrix renormalization group (DMRG) [21]. With controlled error and great computational efficiency, the DMRG can approximate the ground state and low-lying excited states of 1D and quasi-1D systems, such as chains and ladders. It does so by truncating the many-body Hilbert space to include only the most relevant degrees of freedom, thus keeping a controlled computational scaling as the size of the system grows.

Nowadays, a very efficient and useful implementation is conducted with tensor networks, where the physical system is expressed as a matrix product state. The basic idea is to represent the wave function as a tensor with as many indexes as the system has degrees of freedom, and then split this tensor in a product of many tensors, one for each site. Each of these tensors will then hold a physical index, that is, an index associated with the physical degrees of freedom of that site (for instance, spin up or down), and bond indexes to connect it to the rest of the chain [12].

Calculations with tensor networks usually involve contractions between the tensors, which are relatively cheap computationally [22]. Also, as we will see, truncations can be done to simplify the system without incurring in large computational errors.

1.3 Dissertation Outline

The remainder of this dissertation is divided as follows:

- **Chapter 2:** Here, we discuss what is the role of topology in condensed matter, and present some historically relevant models leading to the Kane-Mele-Hubbard model. We then analyze the current literature results on this model.
- **Chapter 3:** In this chapter, we delve into the computational methods used in this work. We start by introducing the original formulation of the DMRG algorithm.

Then, we explain what are tensor networks and matrix product states and the advantages of this approach when carrying out computations of quantum many-body systems. By the end of the chapter, we also cover how the DMRG algorithm works in this framework and how to calculate the entanglement entropy.

- **Chapter 4:** The main results of the work are presented here. We explain how to convert our physical system to an equivalent one-dimensional chain ready to be described as a matrix product state. Then, we expose the results of the numerical calculations conducted, specifically showing the finite-size scaling for the ground state energy, appearance of edge states on the system and the entanglement entropy as a clue to the topological phase transition.
- **Chapter 5:** Finally, we present our conclusions, as well as expose possibilities for further developments.

Chapter 2

Topological phases in Condensed Matter systems

In this chapter, we will discuss the role of topology in condensed matter physics and define what is a topological insulator. Then, we will review how topological insulators were first introduced and show the evolution of some physical models presenting topologically distinct phases. Finally, we will introduce the Kane-Mele-Hubbard model, which is the focus of this work, and examine its phase diagram.

2.1 Topological Insulators

In mathematics, topology can be described as the study of geometrical properties of objects subject to continuous deformations [23]. For instance, as seen on Figure 2.1, a sphere can be continuously, or smoothly, deformed into a "cup", but it cannot be smoothly turned into a "mug", because the "mug" has a hole. This means a sphere and a "cup" are topologically equivalent, while a "mug" is topologically distinct from both.

In this scenario, the number of holes (or genus, if we are being mathematically precise) can take the role of the topological invariant of the system. If it remains unchanged when deforming the system, no topological phase transitions have occurred. On the other hand, if the number of holes changes when deforming the system, this means a topological phase transition took place.

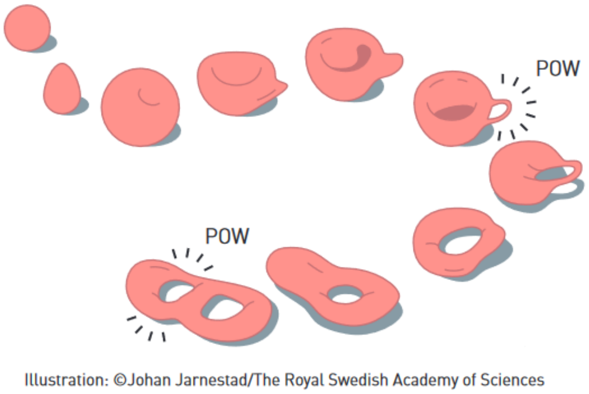
POW
POW
Illustration: ©Johan Jarnestad/The Royal Swedish Academy of Sciences

Figure 2.1: Figure from [15]. Representation of topological phase transitions of closed 2-dimensional surfaces in 3 dimensions.

The same notion of smooth deformations can be applied to the electronic band theory. Traditionally, insulators are materials that present an energy gap between their valence and conduction bands. Therefore, two insulators can be considered topologically equivalent if slow, adiabatic changes to the Hamiltonian when turning one insulator into the other maintain the gap open at all times. This, of course, means that if the gap is closed at some point, the two insulators are topologically distinct, which signals the presence of a topological phase transition [23].

2.2 From QHE to the Kane-Mele model

The Integer Quantum Hall Effect (QHE), discovered in the 1980's, nicely illustrates, in a dramatic way, how topology can play a key role in the properties of a condensed matter system. K. von Klitzing and his collaborators found the quantized Hall conductivity to be proportional to e^2/h [16]. The integer proportionality factor was later shown by Thouless, Kohmoto, Nightingale and den Nijs to be a topological invariant called Chern number (or TKKN invariant) [24], which can be thought of as the number of electrons transported in each cycle of a topological charge pump [23].

2.2.1 Haldane model

The discovery of the QHE led researchers to further explore topological phases of matter. In 1988, F. Duncan Haldane proposed a model of spinless particles in a honeycomb lattice presenting conductance quantization similar to that of the QHE [25]. His idea was to have a model where time-reversal and inversion symmetries are broken, the former due to the presence of a space-varying magnetic field and the latter due to different on-site energies for each triangular sublattice, as represented on Figure 2.2.

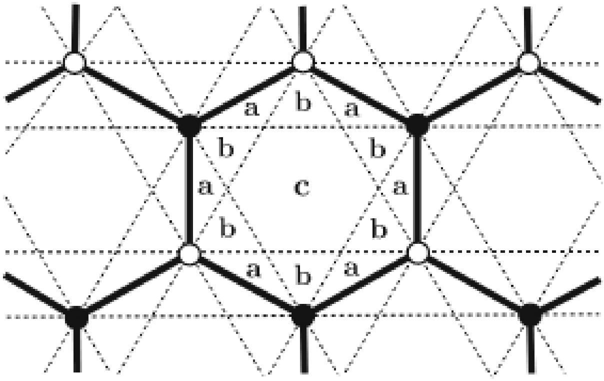

Figure 2.2: Figure from [17]. The Haldane model. Dots with different colors (black or white) are from different sublattices, with different on-site energies. Areas a have magnetic flux ϕ, whereas areas b have magnetic flux $-\phi$ and area c has no magnetic flux. This way, the net flux through the unit cell is zero.

Haldane's model includes opposite on-site energies $+M$ and $-M$ for each sublattice. It also includes a first neighbor hopping t_1 and a second neighbor hopping t_2. This second-neighbors term acquires a phase of $e^{i\phi}$ due to the magnetic flux [17]. Thus, the Hamiltonian can be expressed as

$$H_{Haldane} = -t_1 \sum_{\langle i,j \rangle} c_i^\dagger c_j - t_2 \sum_{\langle\langle i,j \rangle\rangle} e^{i\phi_{ij}} c_i^\dagger c_j + M \sum_i \epsilon_i c_i^\dagger c_i \,, \tag{2.1}$$

where $\phi_{ij} = \pm\phi$ depending on the direction of the hopping and $\epsilon_i = \pm 1$ depending on the sublattice.

Equation (2.1) describes a two-band Hamiltonian. If we consider the case where $|t_2/t_1| < 1/3$, the bands will touch exactly at the vertices of the hexagon formed by the Brillouin zone, but only if $M = \pm 3\sqrt{3} t_2 \sin\phi$. The Hall conductance can then be calculated using the Chern number, via the relation $\sigma_H = n_c \frac{e^2}{h}$. For this system, the Chern number is given by

$$n_c = \frac{1}{2}\left[\text{sgn}(M - 3\sqrt{3}t_2 \sin\phi) + \text{sgn}(-M - 3\sqrt{3}t_2 \sin\phi)\right] \,, \tag{2.2}$$

so it can only take the values of ± 1 or 0. These phases are shown in Figure 2.3.

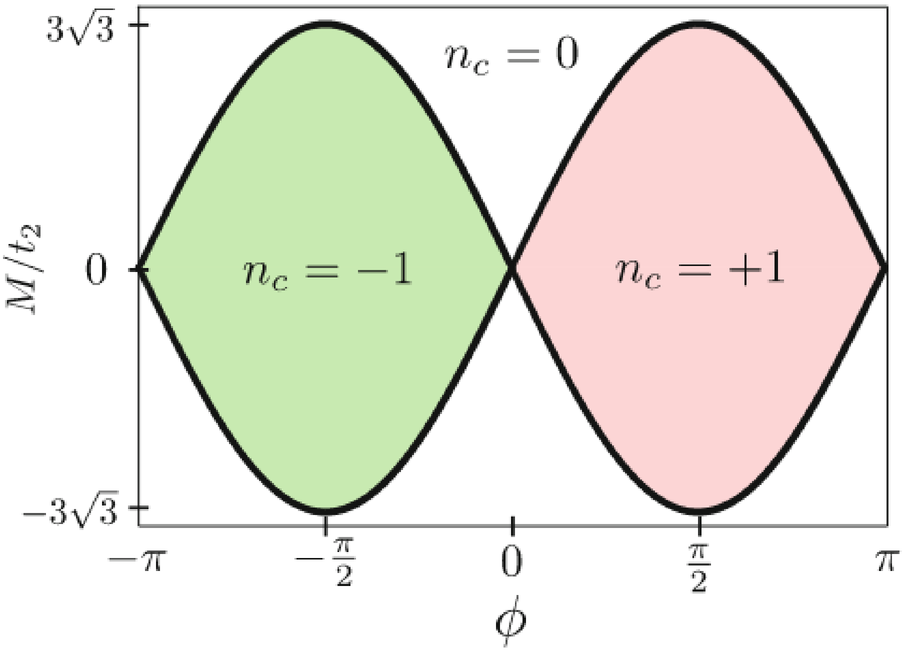

Figure 2.3: Figure from [17]. Phase diagram of the Haldane model.

2.2.2 Kane-Mele model

Haldane's work created the grounds for C. Kane and E. Mele to develop their own model presenting interesting topological properties, in 2005 [10] [18]. This model is largely responsible for the current resurgence in the study of topological insulators.

The Kane-Mele model was created to describe graphene, as it consists of a system of electrons in a honeycomb lattice, taking into account spin-orbit interactions (connecting sites in the same sublattice) instead of a magnetic flux. Thus, it preserves time-reversal symmetry. This model predicted the phenomenon called Quantum Spin Hall Effect (QSHE), which causes the appearance of a topologically non-trivial phase. The QSHE can be thought of as the transport of electrons with different spins in different directions on the edges of the system, in a way that there is no net charge current, but only spin currents around the system [17].

The Hamiltonian of the Kane-Mele model can be written as

$$H_{\text{KM}} = t\sum_{\langle i,j\rangle} c_i^\dagger c_j + i\lambda_{SO}\sum_{\langle\langle i,j\rangle\rangle} \nu_{ij} c_i^\dagger s_z c_j + i\lambda_R \sum_{\langle i,j\rangle} c_i^\dagger (\mathbf{s}\times\mathbf{d}_{ij})_z c_j + \lambda_\nu \sum_i \xi_i c_i^\dagger c_i\,, \tag{2.3}$$

where t is the first-neighbor hopping term, $c_i^\dagger = (c_{i,\uparrow}^\dagger, c_{i,\downarrow}^\dagger)$, λ_{SO} is the spin-orbit coupling, $\nu_{ij} = \frac{2}{\sqrt{3}}(\mathbf{d}_i \times \mathbf{d}_j)_z = \pm 1$ (considering $\mathbf{d}_i$ and $\mathbf{d}_j$ unit vectors along the two bonds the electron goes through when going from site j to site i), s_i are the Pauli matrices, λ_R is the Rashba spin-orbit coupling and the last term is an on-site energy with $\xi_i = \pm 1$ depending on the sublattice.

This model presents 4 energy bands. If there is no Rashba coupling, the z-component of the spin is a good quantum number and the total Hamiltonian can be written as a sum of the spin up and spin down Hamiltonians. In this scenario, the energy gap has a magnitude of $|6\sqrt{3}\lambda_{SO} - 2\lambda_\nu|$, and there is a Chern number for each spin. For $\lambda_\nu > 3\sqrt{3}\lambda_{SO}$, both Chern numbers will be zero. However, for $3\sqrt{3}\lambda_{SO} > \lambda_\nu$, the Chern numbers for each spin s become $n_s = \text{sgn}(s\lambda_{SO})$. Summing both Chern numbers in this case, we will always have $n_+ + n_- = 0$, but their difference yields $n_+ - n_- = \pm 2$. This shows that if $3\sqrt{3}\lambda_{SO} > \lambda_\nu$, we will have the QHE happening for each spin in different directions, thus creating the QSHE.

In the case where $\lambda_R \neq 0$, the total Hamiltonian cannot be expressed as the sum of Hamiltonians of each spin, as the electrons will be mixed. Therefore, we cannot define a Chern number for each spin. What Kane and Mele did instead was to introduce another topological invariant called Z_2 [10]. Either way, the Rashba coupling doesn't close the bulk gap, so it won't affect the appearance of edge states on the system.

Considering a strip sample with periodic boundary conditions in the x-direction, the energy dispersion can be calculated as a function of $k_x a$. As seen in Figure 2.4, there are two phases: one with a pair of bands connecting the conduction and valence bands, and one where the bands do not connect.

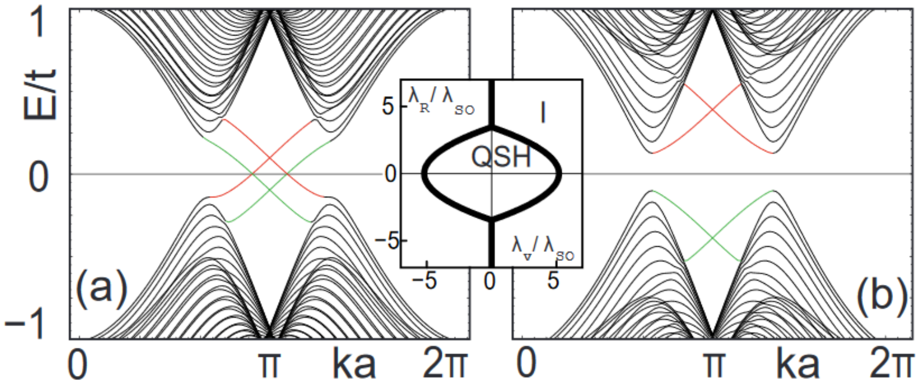

Figure 2.4: Figure from [10]. Energy bands for 1D strip. In both cases we have $\lambda_{SO} = 0.06t$ and $\lambda_R = 0.05t$, but (a) shows the QSHE phase with $\lambda_\nu = 0.1t$, while (b) shows a trivial insulator with $\lambda_\nu = 0.5t$. The inset shows a phase diagram for $0 < \lambda_{SO} \ll t$.

As the system has an energy gap in the bulk, these connecting bands can only be edge states.

2.3 Electronic interactions and the Kane-Mele-Hubbard model

In this work, we will use a simplified version of the Kane-Mele model as a basis to write the Kane-Mele-Hubbard model, in order to focus on the study of the effects of electronic interactions. The Kane-Mele terms we will use, with a slight change in notation to facilitate the implementation of the tensor network-based DMRG algorithm, are

$$H = -t \sum_{\langle \mathbf{i},\mathbf{j} \rangle, s} c^{\dagger}_{\mathbf{i},s} c_{\mathbf{j},s} + i\lambda_{SO} \sum_{\langle\langle \mathbf{i},\mathbf{k} \rangle\rangle, s} c^{\dagger}_{\mathbf{i},s} (\hat{e}_{\mathbf{i},\mathbf{k}} \cdot \sigma)_{s,s'} c_{\mathbf{k},s'} \, , \tag{2.4}$$

where σ is a vector of the Pauli matrices and, in a vector notation, **j** is the position of a nearest-neighbor to a site in position **i**, while $\mathbf{k} \equiv \mathbf{i} + \mathbf{v}_1 + \mathbf{v}_2$ is the position of a next-nearest-neighbor to site **i**.

As defined, the vectors $\mathbf{v}_1$ connect site **i** with its nearest-neighbors **j** and the vectors $\mathbf{v}_2$ connect site **j** to site **k**. This way, $\hat{e}_{\mathbf{i},\mathbf{k}} \equiv \mathbf{v}_1 \times \mathbf{v}_2 / |\mathbf{v}_1 \times \mathbf{v}_2|$ is a vector pointing in the z-direction, orthogonal to the lattice plane, and $\hat{e}_{\mathbf{i},\mathbf{k}} \cdot \sigma = \pm\sigma_z$ or 0. Therefore, the sign defining the direction of the positive and negative spin-orbit coupling in the model is dictated by **k**. In Figure 2.5, the positive direction $+i\lambda_{SO}$ is shown by the arrows connecting second neighbors.

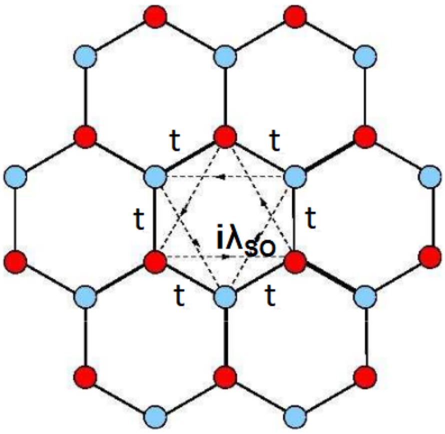

Figure 2.5: Edited figure from [26]. Simplified Kane-Mele model with tight-binding and spin-orbit interactions only. The arrows show the positive direction $+i\lambda_{SO}$ from the sign of $\hat{e}_{\mathbf{i},\mathbf{k}} \cdot \sigma$.

From the inset in Figure 2.4, we can see that this simplified model is in the Quantum Spin Hall phase for any $\lambda_{SO} > 0$. To give an idea on how it can be studied analytically, a deduction of the tight-binding Hamiltonian is presented in Appendix A.

Although most of the efforts directed at studying topological insulators disregard electron interactions, as they might be too meager to have any significant impact on the general behaviour of the system, recently there has been a growing interest on these effects. They might be the key to understanding phenomena such as spin liquid phases in topological insulators [3] [4], topological Mott insulators [5] and topological Kondo insulators [6]. In this work, we are interested in the combination of spin-orbit and correlation effects, and will analyze a system presenting both terms.

Thus, with the addition of an interaction term to the Kane-Mele Hamiltonian, we obtain the Kane-Mele-Hubbard Hamiltonian:

$$H_{\text{KMH}} = -t \sum_{\langle \mathbf{i},\mathbf{j} \rangle, s} c^{\dagger}_{\mathbf{i},s} c_{\mathbf{j},s} + i\lambda_{SO} \sum_{\langle\langle \mathbf{i},\mathbf{k} \rangle\rangle, s} c^{\dagger}_{\mathbf{i},s} (\hat{e}_{\mathbf{i},\mathbf{k}} \cdot \sigma)_{s,s'} c_{\mathbf{k},s'} + U \sum_{\mathbf{i},s} \hat{n}_{\mathbf{i},\uparrow} \hat{n}_{\mathbf{i},\downarrow} \,, \tag{2.5}$$

where U is the Hubbard interaction, representing the Coulombic repulsion for electrons at the same site.

Previous computational efforts to study this model employed Quantum Monte Carlo algorithms in a two-dimensional honeycomb lattice and managed to discover its phase diagram at half-filling [11], as shown in Figure 2.6.

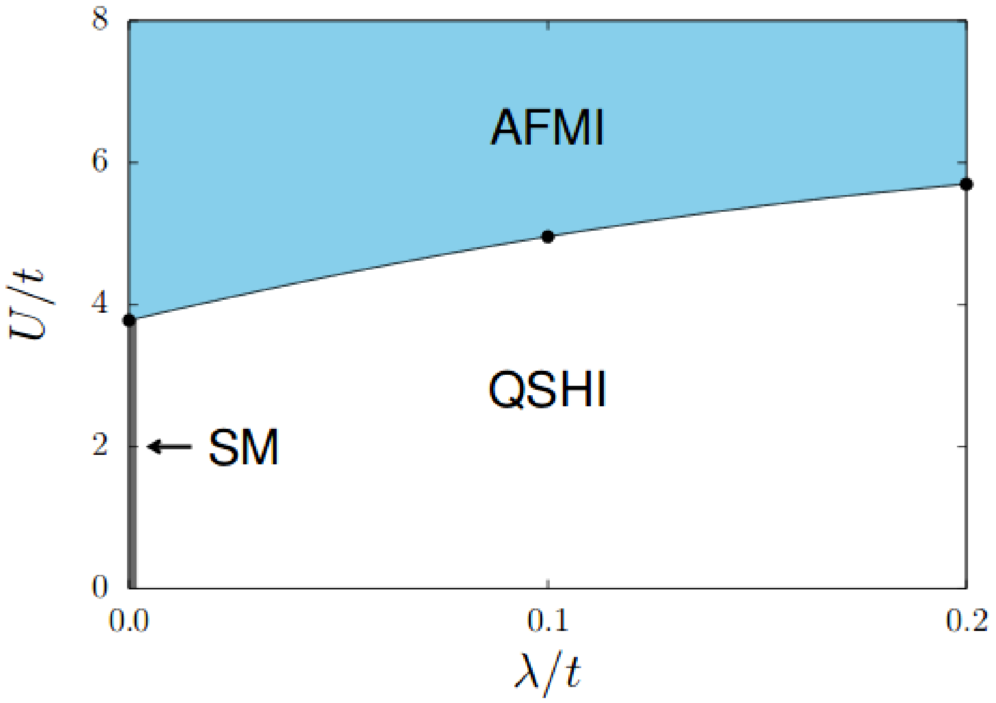

Figure 2.6: Figure from [11]. Phase diagram of the 2D Kane-Mele-Hubbard model, presenting the Semi-Metal (SM), Quantum Spin Hall Insulator (QSHI) and Antiferromagnetic Insulator (AFMI) phases.

As we can see in Figure 2.6, there are three phases in the two-dimensional model: semi-metal, quantum spin hall insulator (or topological insulator) and Mott insulator (which, in this case, presents antiferromagnetic order).

The semi-metal phases appears only for $\lambda = 0$ and low values of U. It is created by a small overlap between conduction and valence bands, due to the fact that the Coulombic repulsion in each site is not strong enough to completely stop electrons from hopping from site to site. On the other hand, if U is large enough, it becomes energetically advantageous for electrons to be localized in their sites. Thus, a Mott insulator phase is created, where there won't be electrical conduction because the repulsion between electrons is too strong for them to be able to hop to another occupied site.

It is interesting to notice how the critical value of U for the transition to a Mott insulator grows alongside the value of λ. This exemplifies the importance of the spin-orbit coupling in the maintenance of a topological insulator phase. In Chapter 4, we will see how the quasi-1D Kane-Mele-Hubbard ladders present a behavior similar to this of the 2D model.

Chapter 3

DMRG and the tensor network matrix product state formalism

In this chapter, we will introduce the density matrix renormalization group (DMRG) algorithm as proposed by Steven White [21]. From there, we will move on to the more modern DMRG implementation via tensor networks, which is the one employed in this work. We will cover how tensor networks can be used to represent matrix product states and what are the advantages of using such states. We will then explain how, in this setting, we can implement the DMRG algorithm and calculate the entanglement entropy of systems. Most of the information here regarding DMRG can be seen in more detail in Chapter 2 of *Strongly Correlated Systems: Numerical Methods* [27], written by Adrian Feiguin, while the base for the tensor networks' sections can be found in the lecture notes of E. Miles Stoudenmire's course on Tensor Networks and Applications [28].

3.1 Density matrix renormalization group algorithm

Introduced by S. White in 1992 [21], the density matrix renormalization group (DMRG) algorithm is a variational method to compute the ground state and low-lying excited states of many-body systems. To do so, it truncates the Hilbert space in such a way that it allows high computational efficiency with controlled error.

Broadly speaking, the original DMRG algorithm implementation consists on calculating the reduced density matrix in each iteration and reducing the degrees of freedom of the system, keeping only the most important ones to approach the ground state. It has been used with great success to study properties of spin chains, such as Ising and Heisenberg models [27].

Even though in this work we will not be using the original implementation of the algorithm, but a highly-efficient version of it based on tensor networks, the way the algorithm works is basically the same [14], so we will first cover the original implementation and then move on to the tensor network formalism.

3.1.1 Motivation: truncated diagonalization

In order to motivate the discussion, let us consider a one-dimensional chain of quantum spins, with interactions given by the Heisenberg Hamiltonian. If we consider only two spins, the Hamiltonian has the form

$$H_2 = S^z \otimes S^z + \frac{1}{2}[S^+ \otimes S^- + S^- \otimes S^+] \,, \tag{3.1}$$

where operators S^z and $S^\pm$ are single spin operators (2 × 2 matrices) acting on one site only. This means that if they are to the left side of the Kronecker product $\otimes$, they are acting on the left site, whereas they act on the right site if they are to the right of $\otimes$. In matrix form, H_2 is 4 × 4.

If we are interested in studying many-body systems, we need to add more spins to the chain. To add a third spin to the right of the existing chain, we can start from Equation 3.1 and write the new 8 × 8 Hamiltonian as follows:

$$H_3 = H_2 \otimes \mathbf{1} + \tilde{S}_2^z \otimes S^z + \frac{1}{2}[\tilde{S}_2^+ \otimes S^- + \tilde{S}_2^- \otimes S^+]\,, \tag{3.2}$$

where $\mathbf{1}$ is the identity matrix and tilde operators $\tilde{S}_2^z$ and $\tilde{S}_2^\pm$ are defined as

$$\tilde{S}_2^z = \mathbf{1} \otimes S^z\,, \tag{3.3}$$

$$\tilde{S}_2^\pm = \mathbf{1} \otimes S^\pm\,. \tag{3.4}$$

Clearly, this leads to a recursive way to create an Hamiltonian with as many spins as desired:

$$H_i = H_{i-1} \otimes \mathbf{1} + \tilde{S}_{i-1}^z \otimes S^z + \frac{1}{2}[\tilde{S}_{i-1}^+ \otimes S^- + \tilde{S}_{i-1}^- \otimes S^+]\,. \tag{3.5}$$

In order to treat this many-spins problem, one can diagonalize the Hamiltonian and find its eigenvectors and eigenvalues. However, as the size of the system grows, the matrix size will increase as well. For a system of N spins, the Hamiltonian will have size $2^N \times 2^N$. Therefore, for large systems, exact diagonalization becomes an extremely costly process.

One idea to reduce the computational cost would be cutting some of the less relevant eigenstates of the system. To do so, consider the Hamiltonian is diagonalized to obtain the ground state $|\Psi\rangle$:

$$|\Psi\rangle = \sum_{s_1,\cdots,s_N} a_{s_1,\ldots,s_N} \left|s_1,\cdots,s_N\right\rangle\,, \tag{3.6}$$

where the sum covers all configurations for all N spins. The square modulus of the coefficients $a_{s_1,\cdots,s_N}$ represent the probability the system will be found in that particular state. Therefore, if we truncate the basis to leave only the states with the largest weights $|a_{s_1,\cdots,s_N}|^2$, we could find a decent approximation to our system, while being able to represent it with a smaller matrix. However, many states with small coefficients would be lost, and if we are not careful we could lose interesting properties of the system in this process.

Luckily, we can always choose whatever basis we want to represent the ground state, just by performing rotations. Thus, if we find a basis where the weights are concentrated in very few states, we can reduce the loss of information when truncating the system. One idea to perform this would be choosing to remove the most energetic states.

If we consider the recursive Hamiltonian creation process from Equation (3.5), we can decide a maximum number of states m we want to keep while increasing the number of spins. When the basis dimension becomes larger than m, we perform the truncation by diagonalizing the Hamiltonian and only keeping the m lowest eigenvalues, representing the least energetic states. Therefore, the Hamiltonian is being rotated to a new basis with every spin added after the system reaches dimension m, and then it gets truncated.

Although this approach of discarding high-energy states has its uses, it does not perform well for strongly correlated many-body systems [27]. For such systems, what works best is truncating the reduced density matrix, as we will soon see.

3.1.2 Truncation based on proximity to ground state

In order to understand this new truncation, we will now consider two blocks of spins in a Heisenberg chain instead of just one. We can grow the blocks at the same time using the recursive mechanism described by Equation (3.5). The block to the left receives a new site to its right, while the block to the right receives a new site to its left. The ground state can be written as

$$|\Psi\rangle = \sum_{i,j} \Psi_{i,j} |i\rangle |j\rangle \ , \tag{3.7}$$

where i (j) is a coefficient for the sites in the left (right) block.

After the system reaches the size of the maximum number of states m we want to keep, we wish to rotate the left block from basis $|i\rangle$ to a new basis $|\alpha\rangle$, creating a truncated approximation

$$|\tilde{\Psi}\rangle = \sum_{\alpha=1}^{m} \sum_{j} \Psi_{\alpha j} |\alpha\rangle |j\rangle \ , \tag{3.8}$$

in such a matter that we minimize the value of

$$|\, |\Psi\rangle - |\tilde{\Psi}\rangle \,|^2 . \tag{3.9}$$

The question is then how to choose this $|\alpha\rangle$ basis, and to answer it we need to explore reduced density matrices and the Schmidt decomposition of quantum states.

3.1.3 Density matrices

The density matrix of a quantum system is a generalization of the wave function as a way to characterize the system. Its definition is

$$\rho = |\Psi\rangle \langle\Psi| \ . \tag{3.10}$$

If the system is divided in sub-partitions A and B, we can calculate the reduced density matrix for each partition by taking partial traces over ρ

$$\rho_A = \mathrm{tr}_B\, \rho, \quad \rho_B = \mathrm{tr}_A\, \rho\, . \tag{3.11}$$

The reduced density matrix of each partition fully characterizes that partition. Say we want to calculate an observable $\hat{O}$ that acts on partition A and not on partition B. Instead of doing it the usual way, $\langle\Psi|\,\hat{O}\,|\Psi\rangle$, we can just calculate a trace:

$$\langle\hat{O}\rangle = \mathrm{tr}[\rho_A\hat{O}]\,. \tag{3.12}$$

3.1.4 Singular value decomposition and Schmidt decomposition

The singular value decomposition (SVD) is a particular way to factorize a rectangular matrix. We can define it as

$$M = U\Lambda V^\dagger\,, \tag{3.13}$$

where M is a rectangular matrix of dimensions $D_A \times D_B$, Λ is a $D_B \times D_B$ diagonal matrix, U has dimensions $D_A \times D_B$ and V has dimensions $D_B \times D_B$. U and V are unitary matrices, which means that

$$UU^\dagger = \mathbf{1}, \quad VV^\dagger = \mathbf{1}\,. \tag{3.14}$$

Another property of U and V is that their columns are orthonormal vectors, thus we can consider them rotation matrices.

The diagonal entries on the Λ matrix are real, positive semi-definite numbers, ordered from the largest to the lowest value. They are called singular values and represent the most relevant information of the original matrix.

If we apply an SVD to the coefficients of the wave function in Equation (3.7), we get

$$|\Psi\rangle = \sum_i^{D_A}\sum_j^{D_B}\sum_\alpha^{r} U_{i\alpha}\lambda_\alpha V^*_{\alpha j}\,|i\rangle\,|j\rangle\ , \tag{3.15}$$

where λ_α are the singular values of Ψ_{ij} and r is the smallest dimension size between D_A and D_B. We can define the following states, which determine a new orthonormal basis:

$$|\alpha\rangle_A \equiv \sum_{i}^{D_A} U_{i\alpha} |i\rangle \tag{3.16}$$

and

$$|\alpha\rangle_B \equiv \sum_{j}^{D_B} V_{\alpha j}^{*} |j\rangle \ . \tag{3.17}$$

This basis is called Schmidt basis. In this notation, Eq (3.15) becomes

$$|\Psi\rangle = \sum_{\alpha} \lambda_\alpha |\alpha\rangle_A |\alpha\rangle_B \tag{3.18}$$

and the reduced density matrix can be written as

$$\rho_A = \sum_{\alpha} \lambda_\alpha^2 |\alpha\rangle_{A\,A} \langle\alpha| \ , \tag{3.19}$$

from where we can see the eigenvalues of ρ_A are the square of the singular values of Ψ_{ij} and the Schmidt basis represent the eigenvectors of ρ_A.

With these notions, we can tackle the question of how to find the truncated approximation $|\tilde{\Psi}\rangle$ from Equation (3.8) as a low-ranking approximation problem. If we rename the eigenvalues of ρ_A as

$$\omega_\alpha \equiv \lambda_\alpha^2 \tag{3.20}$$

and place them in decreasing order, we will find

$$|\,|\Psi\rangle - |\tilde{\Psi}\rangle\,|^2 = \sum_{m+1}^{r} \omega_i \,, \tag{3.21}$$

showing that using the m eigenvectors of the reduced density matrix with the m largest eigenvalues is the optimal basis for reducing losses during the truncation.

3.1.5 Infinite-size DMRG

We now have all we need to cover the steps of the infinite-size DMRG algorithm. Its idea is to grow the left and right blocks by adding one site to each, and once we reach the maximum number of states m we want to keep, start applying truncations to the reduced density matrices of the blocks until either the desired system size is reached or the error is below an arbitrary tolerance. The steps are represented in Figure 3.1, and can be described as follows.

First, we need to create all operators for the single-site Hamiltonian and for interactions between a site and the rest of the system. Then, we grow the blocks by adding one site to the right of the left block and another site to the left of the right block, similar to the procedure described by Equation (3.5). If we call the dimension of a single site d, the blocks will eventually become larger than $d \times m$ and at this point we need to start truncating the reduced density matrices.

To perform the truncation, we start by diagonalizing the full Hamiltonian of the two blocks to obtain the ground state. Then, we calculate and diagonalize the reduced density matrices of each block, truncating the basis and leaving only the m eigenvectors with largest eigenvalues. After that, we rotate the Hamiltonian and the operators to this new basis, as in Equation (3.8). This process can be repeated until the system is at the desired size or the error is smaller than an arbitrary tolerance value.

At first, it was thought that infinite-size DMRG would be a good approximation to the thermodynamic limit. However, nowadays it is known that the best way to approach it is by using the finite-size algorithm [27].

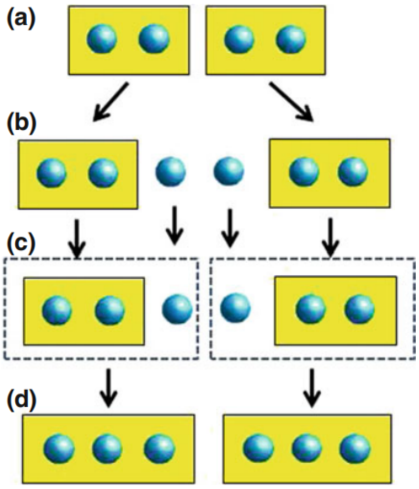

Figure 3.1: Figure from [27]. Depiction of the block-growth process in the infinite-size DMRG. Starting from the blocks on step (**a**), we add a new site to each block (**b**), obtain the ground state of the whole system (**c**) and calculate the reduced density matrices to rotate the system to the new basis keeping only the m largest eigenvalues of the density matrices, generating a new block (**d**) for the next iteration.

3.1.6 Finite-size DMRG

The finite-size DMRG algorithm is represented in Figure 3.2. It stars by running the infinite-size algorithm to reach a desired system size. From there, we need to conduct DMRG sweeps from one side of the chain to the other and vice versa.

A sweep from the left side to the right side begins by adding a site to the right of the left block, similar to the infinite-size case. Here, however, the system has a fixed size, so we need to remove the site from the right block, shrinking that block.

Then, we diagonalize the Hamiltonian of the whole system to find the ground state. At this point, we compute and diagonalize the reduced density matrix of the left block, finding its eigenvectors and eigenvalues. The basis is then truncated keeping the m eigenvectors of the reduced density matrix with largest eigenvalues. Finally, the Hamiltonian and the operators of the left block are rotated to the new basis. This process should repeat itself until the right-boundary of the system is reached, completing a sweep from left to right.

When the right-boundary is reached, we start a sweep in the opposite direction, growing the right block and shrinking the left one. Sweeps should be re-iterated until the change in energy gets lower than an arbitrary tolerance.

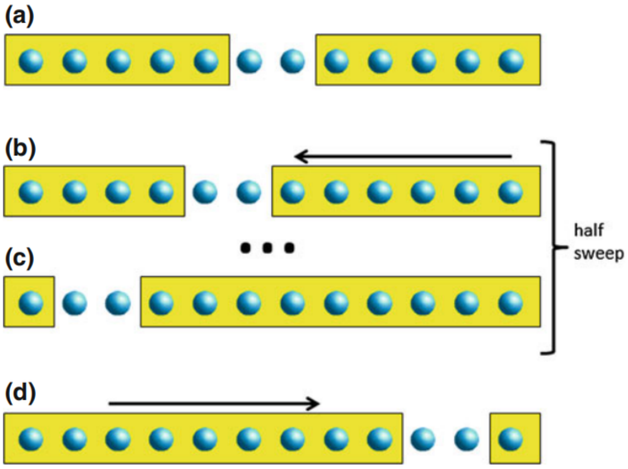

Figure 3.2: Figure from [27]. Depiction of the sweeps in the finite-size DMRG algorithm. Starting from the blocks from the infinite-size DMRG, we conduct sweeps from one direction to the other and vice versa, in a way that as one block grows, the other shrinks.

The sweeping process works as a self-consistent loop to improve the solution after each iteration. The finite-size DMRG can be seen as a variational method in which parameters are changed in order to minimize an energy functional [27].

3.2 Matrix product states as tensor networks

Modern implementations of DMRG are carried out via tensor networks (TN), and a matrix product state (MPS) representation of the systems studied is used. This perspective allows a clearer understanding of the reduction of complexity for many-body systems, as well as it facilitates the calculation of physical quantities such as expectation values and entanglement entropy. The TN/MPS approach is the one we are going to follow in this work, taking use of a C++ tensor network library called ITensor [9].

To understand how it works, we must first define what is an MPS and why we are using it. Broadly speaking, the MPS is an ansatz for the wave function of the ground-state of many-body systems, and it can be represented as

$$|\Psi_{\text{MPS}}\rangle = \sum_{s_1 \ldots s_N} M_1^{(s_1)} M_2^{(s_2)} \ldots M_N^{(s_N)} \, |s_1 s_2 \ldots s_N\rangle \ , \tag{3.22}$$

where M_n^s are rectangular matrices acting on each site (1 to N), with degrees of freedom s (for instance, spin up or down for the particle in each site). The idea is to associate each matrix with a site, while bounds between sites are represented by the indexes of the matrices.

Such a wave function is easily represented as a TN. Let's take an example with a 5-site spin chain:

$$\begin{aligned} \Psi^{s_1 s_2 s_3 s_4 s_5} &= M_1^{s_1} M_2^{s_2} M_3^{s_3} M_4^{s_4} M_5^{s_5} \\ &= \sum_{\{\alpha\}} M^{s_1}_{\alpha_1} M^{s_2}_{\alpha_1 \alpha_2} M^{s_3}_{\alpha_2 \alpha_3} M^{s_4}_{\alpha_3 \alpha_4} M^{s_5}_{\alpha_4} \\ &= \end{aligned}$$

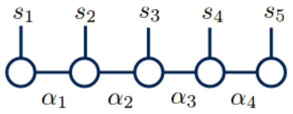

Figure 3.3: Figure from [28]. 5-site MPS and its representation as a TN.

In Figure 3.3, we can see a pictorial representation of an MPS as a TN. The tensors are the circles, while each of their indexes are the connections coming out of the circle. The rank of each tensor can be determined by the amount of connectors coming out of it. For instance, the first tensor on the left of the chain has a bond index α_1, connecting it to its neighbour, and a physical index s_1, representing the spin of the particle in that site. Sites on the middle of the chain will have tensors with three indexes instead of two, because they have two neighbours and one physical index. This means these central tensors have rank 3, while the edge ones have rank 2.

The bonds between two tensors can be removed by contracting the tensors, turning them into just one tensor, as shown in Figure 3.4.

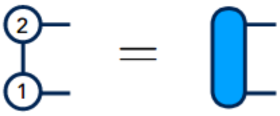

Figure 3.4: Figure from [28]. Contraction of two tensors in a TN.

Thus, we can get the full many-body wave function back from our MPS at any time, as a large tensor with physical indexes only, as represented in Figure 3.5.

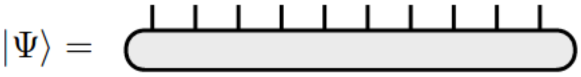

Figure 3.5: Figure from [28]. 10-site wave function as only one tensor.

However, what favours the use of MPS is the computational efficiency. To illustrate this, let us consider a calculation of the norm of a many-body wave function. While working with the full wave function, we would have something like:

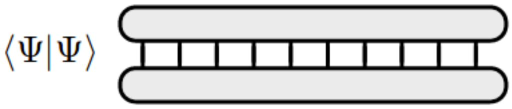

$$= \sum_{\{s\}} \Psi^{s_1 s_2 s_3 s_4 s_5 s_6 s_7 s_8 s_9 s_{10}} \bar{\Psi}_{s_1 s_2 s_3 s_4 s_5 s_6 s_7 s_8 s_9 s_{10}}$$

Figure 3.6: Figure from [28]. Norm of the 10-site wave function.

In Figure 3.6, we have constructed $\langle\Psi|$ as the complex conjugate of $|\Psi\rangle$, and connected the physical indexes so we can calculate the norm. This procedure would require summing, in this 10-site example, 2^{10} terms.

On the other hand, using MPS we can get the same results just by doing cheaper tensor multiplications, as we can see in Figure 3.7.

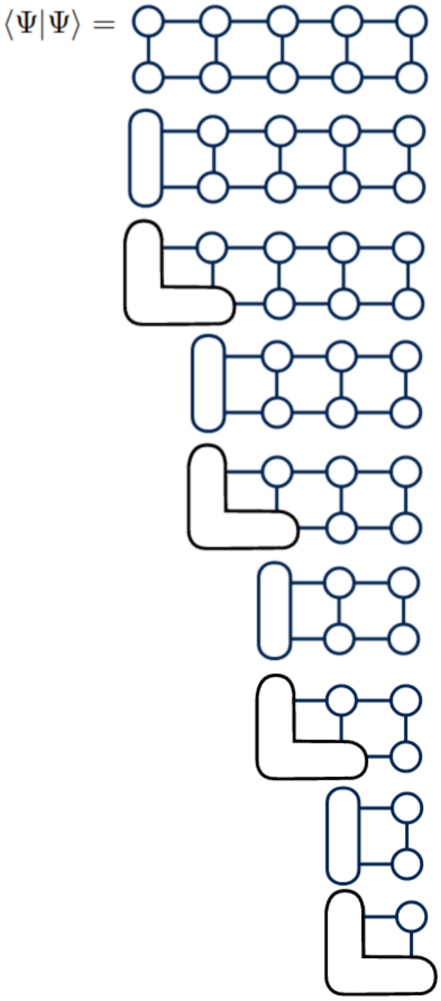

Figure 3.7: Figure from [28]. Calculating the norm of Ψ with MPS.

The scaling for tensor contractions is given by multiplying the dimensions of the indexes of the tensors involved. If we call the dimension of bond indexes m and of physical indexes d, each contraction conducted has a cost of m^3d [22], as seen on Figure 3.8. Compared to the full wave function calculation, this is much cheaper computationally.

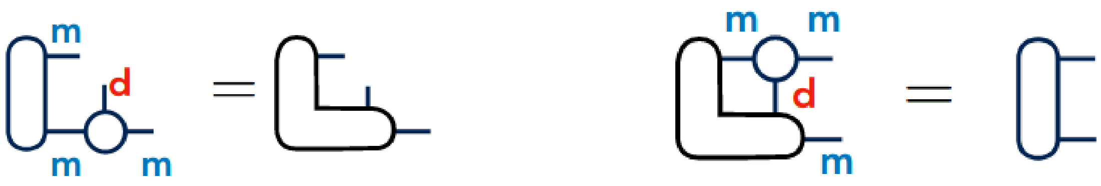

(a) First contraction type

(b) Second contraction type

Figure 3.8: Figure from [28]. Indexes' dimensions for calculation of MPS contractions cost. We can see both types of contractions have the same cost of $m^3 d$.

Another advantage of using MPS is the ability to easily evaluate local and global observables. To do so, we need to understand how to apply operators to wave functions in this tensor network framework.

3.3 Measuring observables

At a first glance, calculating expectation values of operators seems like an almost trivial task with MPS/TN. Suppose we want to calculate the expectation value of a two-site operator A: all we need to do is write the operator as a tensor with the same physical indexes as the sites of the MPS it is acting on and put it in the middle of a norm calculation, as in Figure 3.9.

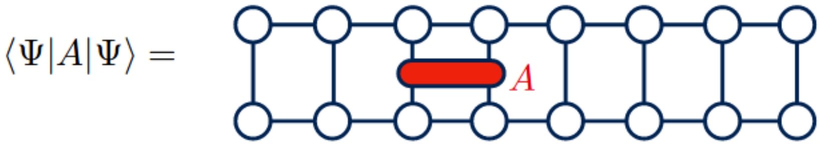

Figure 3.9: Figure from [28]. Expectation value of operator A acting on sites 3 and 4 of a chain.

Using tensor contractions just like in the norm calculation, we can simplify the system, making the process less computationally expensive. The result of the contractions can be seen in Figure 3.10.

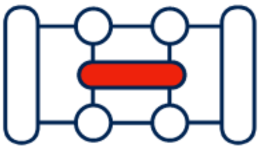

Figure 3.10: Figure from [28]. Contracting tensors from sites outside of the measurement makes the calculation more efficient, just like when calculating the norm.

There is, however, a way to improve the efficiency of these calculations even further, while also keeping high accuracy when truncating the system. In order to discuss this method, it is necessary to discuss SVDs and gauge choices in the MPS setting.

3.3.1 Singular value decomposition and MPS gauge

We have already defined the SVD in Equation (3.13), and in this section we will check how each of the resulting matrices have useful properties for MPS/TN. First of all, for the sake of simplicity we will adopt another notation for the SVD of a rectangular matrix M:

$$M = U\Lambda V\,, \tag{3.23}$$

where Λ is a diagonal matrix, U is a left-orthogonal unitary matrix and V is a right-orthogonal unitary matrix. This means that

$$U^\dagger U = \mathbf{1}, \quad VV^\dagger = \mathbf{1}\,. \tag{3.24}$$

If we consider a generic many-body wave function, we can group its indexes to treat it as a matrix and perform an SVD, as shown in Figure 3.11.

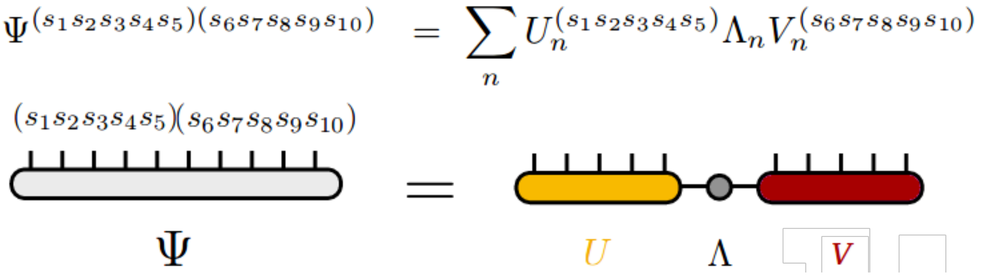
$\Psi^{(s_1s_2s_3s_4s_5)(s_6s_7s_8s_9s_{10})} = \sum_n U_n^{(s_1s_2s_3s_4s_5)}\Lambda_n V_n^{(s_6s_7s_8s_9s_{10})}$
$(s_1s_2s_3s_4s_5)(s_6s_7s_8s_9s_{10})$
Ψ
U
Λ
V

Figure 3.11: Figure from [28]. SVD applied to a wave function and its TN graphical representation.

The color code in Figure 3.11 is the one we are going to follow from now on. A light gray tensor, as the one on the left side of the equation, represents a tensor which did not go through an SVD yet. Yellow and red tensors are, respectively, left-orthogonal and right-orthogonal, while dark gray tensors such as Λ contain the singular values.

But what happens if we want to perform SVD to an MPS? To motivate this discussion, let us check what happens when applying the SVD to a two-site wave function.

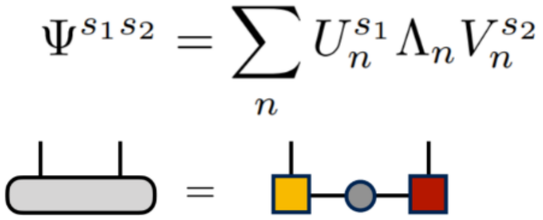
$\Psi^{s_1s_2} = \sum_n U_n^{s_1}\Lambda_n V_n^{s_2}$

Figure 3.12: Figure from [28]. SVD of two-site wave function and its TN graphical representation as an MPS.

In Figure 3.12, we can see that the result of the SVD is an MPS formed by matrices U, Λ and V. So, if we consider a generic MPS, we can contract any two adjacent tensors and perform an SVD to it, and the result will still be an MPS that represents the same physical system.

Then, if after the SVD we contract Λ with V, we can perform another SVD with the site to the right of this new tensor, iteratively creating a chain of unitary tensors to the left or your singular value tensor. This is represented graphically in Figure 3.13. The same can be done the other way around, from right to left, contracting Λ with U and performing SVDs to the left, leaving a chain of unitary tensors to the right.

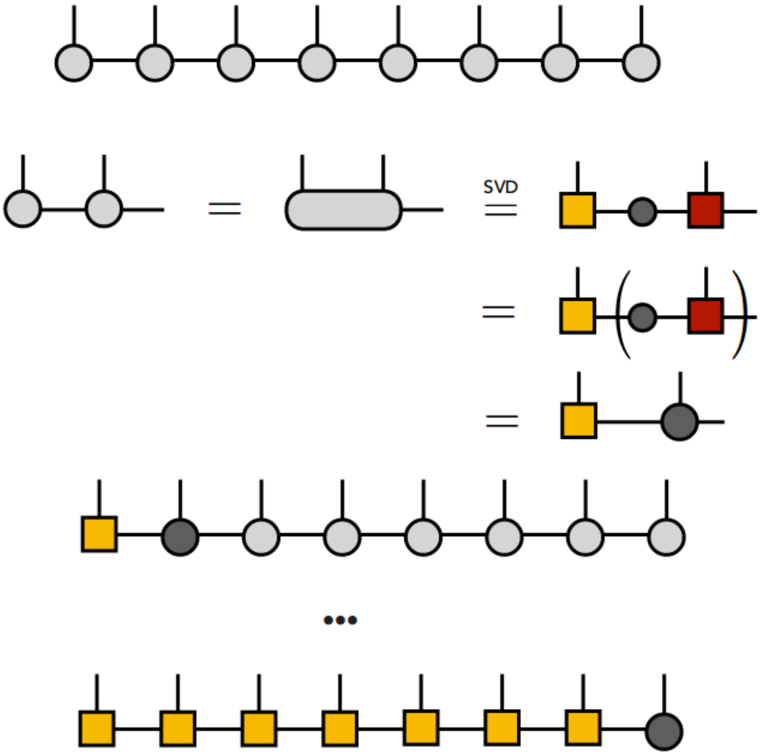

Figure 3.13: Figure from [28]. Iteratively applying SVDs to an MPS will create a chain of unitary tensors.

This procedure can be conducted from both sides simultaneously, leaving the tensor with the singular values of the MPS at any desired site in the chain. In Figure 3.14, for instance, the singular values are stored in the fourth tensor in the chain. The singular values tensor is known as the orthogonality center of the MPS, and the act of choosing its position is called “gauging”.

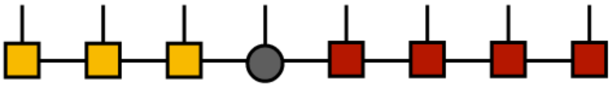

Figure 3.14: Figure from [28]. MPS can be adjusted (gauged) via SVDs so that the tensor with singular values can stay at any position in the chain.

The point of all this is to use the unitary properties to our advantage. We know that U and V have the properties described in Equation 3.24, which we can translate to the TN graphical language as in Figure 3.15.

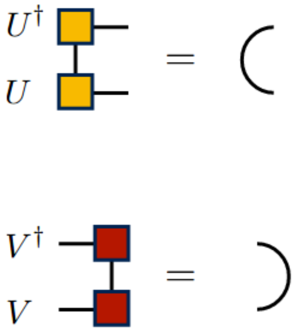

Figure 3.15: Figure from [28]. Orthogonality of U and V in the TN representation.

Therefore, if we want to measure the expectation value of an operator acting on specific sites in the chain, we can do as in Figure 3.16: gauge the MPS so that the orthogonality center is in one of these sites, allowing the cancellation of most of the tensors and leaving us with a much smaller diagram to compute.

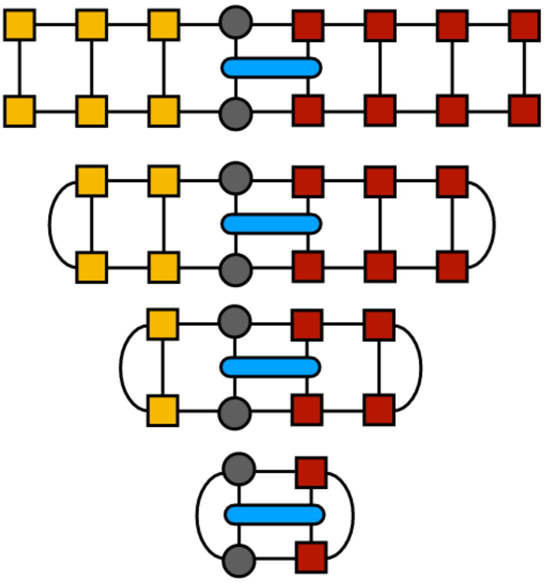

Figure 3.16: Figure from [28]. Using the orthogonality of U and V and the proper gauge of the MPS, the expectation value calculation is much simpler.

3.3.2 Truncating the MPS

Another way to increase computational efficiency when using an MPS is by truncating it in a controlled way. Luckily, this can easily be done with SVDs. As we already mentioned, the singular values that arise from an SVD carry the important information of the original matrix. In the case of a many-body wave function, the singular values represent degrees of freedom of the system. If we remove some of them from our Λ matrix, we will be reducing the degrees of freedom, thus truncating the Hilbert space of the many-body system. To do this in a controlled manner, we can remove just the small singular values from Λ, while keeping the large ones, just like we have seen in Section 3.1. This way, the MPS will remain almost unchanged, but the computational cost of evaluating observables will decrease significantly.

To elucidate the advantage of using truncations, we can take a look at a simple example. Considering the following matrix

$$M = \begin{bmatrix} 0.4358 & 0.2237 & 0.1 \\ 0.4358 & 0.2237 & -0.1 \\ 0.2237 & 0.4358 & 0.1 \\ 0.2237 & 0.4358 & -0.1 \end{bmatrix},$$

by calculating its SVD, we get

$$M = \begin{bmatrix} -0.5 & -0.5 & 0.5 & -0.5 \\ -0.5 & -0.5 & -0.5 & 0.5 \\ -0.5 & 0.5 & 0.5 & 0.5 \\ -0.5 & 0.5 & -0.5 & -0.5 \end{bmatrix} \begin{bmatrix} 0.9327 & 0 & 0 \\ 0 & 0.3 & 0 \\ 0 & 0 & 0.2 \\ 0 & 0 & 0 \end{bmatrix} \begin{bmatrix} -0.7071 & -0.7071 & 0 \\ -0.7071 & 0.7071 & 0 \\ 0 & 0 & 1 \end{bmatrix},$$

where the singular values are 0.9327, 0.3 and 0.2. If we remove the smallest singular value (that is, replace it with a zero in the singular values matrix) and multiply the matrices back together, we will end up with

$$M' = \begin{bmatrix} 0.4358 & 0.2237 & 0 \\ 0.4358 & 0.2237 & 0 \\ 0.2237 & 0.4358 & 0 \\ 0.2237 & 0.4358 & 0 \end{bmatrix}.$$

We can use the square of the norm to calculate the difference between M and M':

$$||M - M'||^2 = 0.04 = (0.2)^2 .$$

We can see the truncation error is determined by the singular value eliminated. Thus, choosing which singular values will be cut, we can control the error of the truncation.

In Section 3.1.4, we have shown how the singular values of a wave function relate to its reduced density matrix: the eigenvalues of the reduced density matrix are the squares of the singular values from applying the SVD to the wave function. So, by applying this singular value truncation to an MPS, what we are doing is no different to the approximation described by Equation (3.8), which minimizes the difference between a true ground state and its approximation.

One thing to keep in mind is that it is important to truncate the MPS only at the orthogonality center. Small local errors at the orthogonality center due to truncation of the MPS carry small global errors to the MPS, while performing truncations away from the orthogonality center can cause large global errors [28].

3.4 DMRG with tensor networks

Now that we have introduced the concept of matrix product states as tensor networks and showed how they can be truncated via singular value decompositions, we are almost ready to discuss the mechanism of the DMRG algorithm. Before that, we will need to take a quick look at matrix product operators.

3.4.1 Matrix product operators

Matrix product operators (MPOs) are operators written in the matrix product formulation. This means that they are a chain of tensors, like an MPS, but with two physical indices: one to connect it to $\langle\Psi|$ and the other to connect it to $|\Psi\rangle$, as seen in Figure 3.17. They are very useful to represent Hamiltonians and are essential to this formulation of the DMRG algorithm, as we will see.

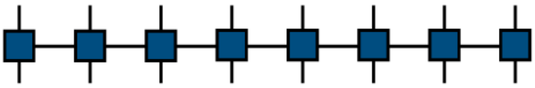

Figure 3.17: Figure from [28]. Graphical representation of an MPO.

The formal definition of an MPO can be written as

$$\hat{O} = \sum_{s,s'} \sum_{b} W^{s_1,s'_1}_{1,b_1} W^{s_2,s'_2}_{b_1,b_2} \cdots W^{s_L,s'_L}_{b_{N-1},1} \, , \tag{3.25}$$

where W are tensors acting on each site i on the chain, with $i = 1$ being the first site the operator acts on and $i = N$ the last one. The indices b represent the bonds between the MPO tensors.

Applying an MPO to an MPS runs as follows

$$\begin{aligned} \hat{O}\,|\Psi\rangle &= \sum_{s,s'} \sum_{a,b} (W^{s_1,s'_1}_{1,b_1} W^{s_2,s'_2}_{b_1,b_2} \cdots)(M^{s'_1}_{1,a_1} M^{s'_2}_{a_1,a_2} \cdots)\,|\mathbf{s}\rangle \\ &= \sum_{s,s'} \sum_{a,b} (W^{s_1,s'_1}_{1,b_1} M^{s'_1}_{1,a_1})(W^{s_2,s'_2}_{b_1,b_2} M^{s'_2}_{a_1,a_2}) \cdots |\mathbf{s}\rangle \\ &= \sum_{s} \sum_{a,b} N^{s_1}_{(1,1),(b_1,a_1)} N^{s_2}_{(b_1,a_1),(b_2,a_2)} \cdots |\mathbf{s}\rangle \ , \end{aligned} \tag{3.26}$$

where

$$N^{s_i}_{(b_{i-1},a_{i-1}),(b_i,a_i)} = \sum_{s'_i} W^{s_i,s'_i}_{b_{i-1},b_i} M^{s'_i}_{a_{i-1},a_i} \tag{3.27}$$

are tensors defining a new MPS after the application of the MPO.

3.4.2 DMRG in the TN/MPS formulation

As Figure 3.18 illustrates, the DMRG algorithm implemented in the ITensor library [9] follows a few steps:

- Write the system as an MPS with well-defined orthogonality center, coupled to the MPO that will be measured (in this case, the Hamiltonian), which in turn shall be coupled to the complex conjugate of the MPS removing the orthogonality center and its nearest neighbor to the right. The reason to remove these sites is that we will focus on solving the eigenvalue problem in the reduced Hilbert space given by the orthogonality center and its neighbor in each step of the algorithm. The procedure to write Hamiltonians as MPOs is described in Refs. [14], [28]. One of the advantages of using the ITensor library is we usually do not have to worry about it, as the library has an internal way to automatically create MPOs based on already-implemented on-site operators, such as the creation and annihilation operators [29].

- Truncate the MPS at the orthogonality center based on the desired number of states m we want to keep. As explained in Section 3.3.2, this is equivalent to the density matrix eigenvectors truncation in the DMRG algorithm described in Section 3.1.

- Contract the tensors to the left and to the right of the chosen site, leaving uncontracted only the tensors at the orthogonality center and their first neighbors to the right.

- Contract the two central MPS tensors with each other. At each step, these are the tensors we will evaluate in order to find a lower energy state. We could use just the orthogonality center, but in the ITensor library both tensors are used at each step in order to increase efficiency [28].

- Solve the eigenvalue problem for the reduced Hilbert space described by the two contracted MPS sites via the Davidson [30] or Lanczos [31] eigensolver algorithms. We are interested in finding the end of the energy spectrum, that is, the lowest energy states, so there is no need to conduct a full exact diagonalization. The idea is that while the matrices outside the orthogonality center are being kept constant, the ones at the orthogonality center will have its entries varied in the process of minimizing $\langle\Psi| H |\Psi\rangle - \lambda \langle\Psi|\Psi\rangle$, allowing us to find a state with lower energy than the current one. Each time this procedure is repeated along the chain, we will get closer to the ground state (or at least to a local energy minimum).

- Split again all tensors, but moving the orthogonality center one site to the side via a new SVD gauging process. A truncation must happen if the number of states is larger than the maximum one we defined (m).

- Redo the process until it gets to the border of the chain, where the calculations will then start to move on the opposite direction.

In this setting, the DMRG sweeps are represented by the repetition of all this steps until a border of the system is reached. Each sweep will bring the system closer to its ground state, so after successive sweeps the DMRG algorithm can bring the system to the ground state with high precision.

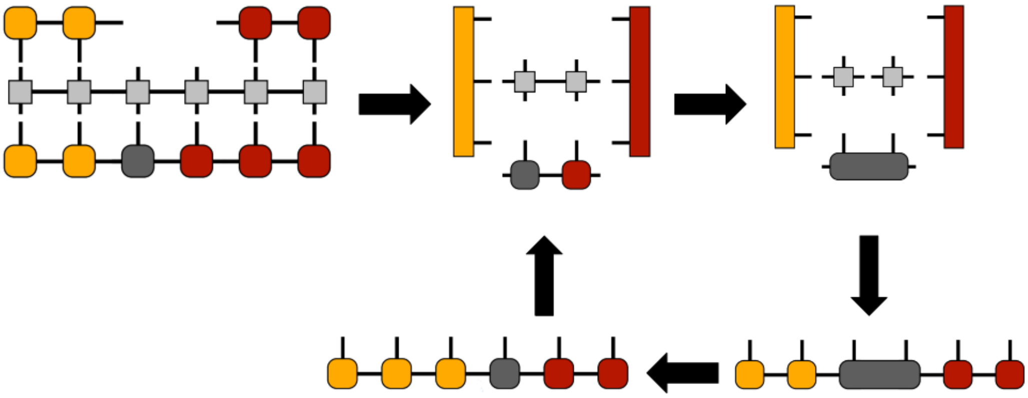

Figure 3.18: Figure from [28]. Steps of the DMRG algorithm implemented via TN/MPS.

3.5 Calculating the entanglement entropy

Aside from the practical calculation of observables and the DMRG implementation, TN/MPS are also very useful to calculate the entanglement entropy of many-body systems. In this section we will discuss what this means and how it can be done.

3.5.1 Entanglement

Given a quantum system with interacting particles, we can say the entanglement between the particles is the amount of information of the whole system that is shared between them. For instance, we can examine two states formed by systems of two spins:

$$|\Psi_1\rangle = |\uparrow\uparrow\rangle + |\uparrow\downarrow\rangle + |\downarrow\uparrow\rangle + |\downarrow\downarrow\rangle\,, \qquad |\Psi_2\rangle = |\uparrow\downarrow\rangle + |\downarrow\uparrow\rangle\ . \tag{3.28}$$

Analyzing $|\Psi_1\rangle$, if we know the state of the first spin, it does not tell us anything about the second spin; it can very well be up or down. On the other hand, if we look at $|\Psi_2\rangle$, knowing the state of any of the spins fully determines the state of the other, as they are always pointing in opposite directions. We call states like $|\Psi_1\rangle$ product states, as the two spins are not entangled and their wave functions can be expressed as a product of each of the spins. States like $|\Psi_2\rangle$ are called maximally entangled states, as the entanglement between the parts allows us to know the state of the whole system just by knowing the state of one of the parts [27].

3.5.2 The von Neumann entropy

One way to quantify the entanglement between partitions of a quantum system is by calculating a quantity called entanglement entropy. From the reduced density matrix defined in Equation (3.11), we can define the entanglement entropy of a system divided in two partitions, A and B, as the von Neumann entropy:

$$S_A = -\mathrm{tr}[\rho_A \log(\rho_A)] = -\sum_\alpha \lambda_\alpha^2 \log(\lambda_\alpha^2)\,, \tag{3.29}$$

where λ_α^2 are the eigenvalues of ρ_A. The idea behind this entropy is that it quantifies the information shared between the two partitions. But how does all this relates to MPS?

Although we could calculate the reduced density matrix in our TN formulation, as in Figure 3.19, where the connecting lines going over partition B represent the partial trace over that partition, there is a simpler way to get the entanglement entropy from an MPS.

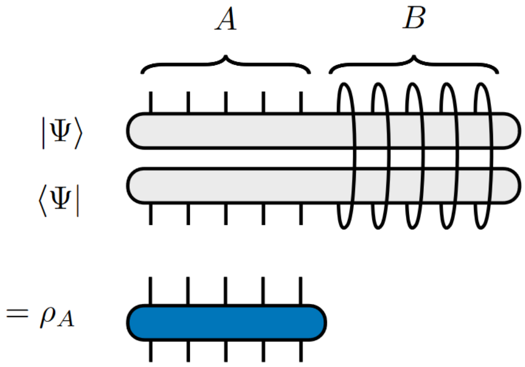

Figure 3.19: Figure from [28]. TN representation of the reduced density matrix. It is obtained after taking the partial trace over one partition of the system.

In section 3.1, we have already seen how the eigenvalues of the reduced density matrix, λ_α^2, are the squares of the singular values λ_α from an SVD of a quantum state. This means that if we want to calculate the entanglement entropy between two partitions of a system, all we have to do is gauge the MPS (as explained in Section 3.3.1) to the site at the division between the partitions, and the SVD procedure employed to perform this task will already provide us with the singular values λ_α we need to calculate the entanglement entropy.

It is important to mention that the entanglement entropy of the ground state of gapped one-dimensional systems with local Hamiltonians usually obeys an area law [27]. The area law states that the entanglement entropy between two partitions of the system grows at the most in the same pace as the boundary between the partitions. For one-dimensional systems divided in two partitions, this means the size of the partitions does not influence the entanglement entropy between them.

Chapter 4

Kane-Mele-Hubbard ladders

In this chapter, we will cover how to represent the Kane-Mele-Hubbard ladders as a one-dimensional chain ready for the DMRG calculations, as well as the numerical results obtained after calculating their ground state. All results presented are considering the system at half-filling, that is, with a number of electrons equal to the number of sites in the chain.

4.1 Representing Kane-Mele-Hubbard ladders in 1D

While most of the research on topological phases of matter is focused on 2D materials, the role of dimensionality in these systems is still largely unexplored. For instance, what happens to the topological phase in quasi-1D structures, such as ladders?

Delving into this question, we focused in studying a honeycomb strip presenting the Kane-Mele-Hubbard Hamiltonian. Since we want to use a TN/MPS approach due to all its advantages mentioned in Chapter 3, it was necessary to use a topologically equivalent version to the system in one dimension, as shown in Figure 4.1.

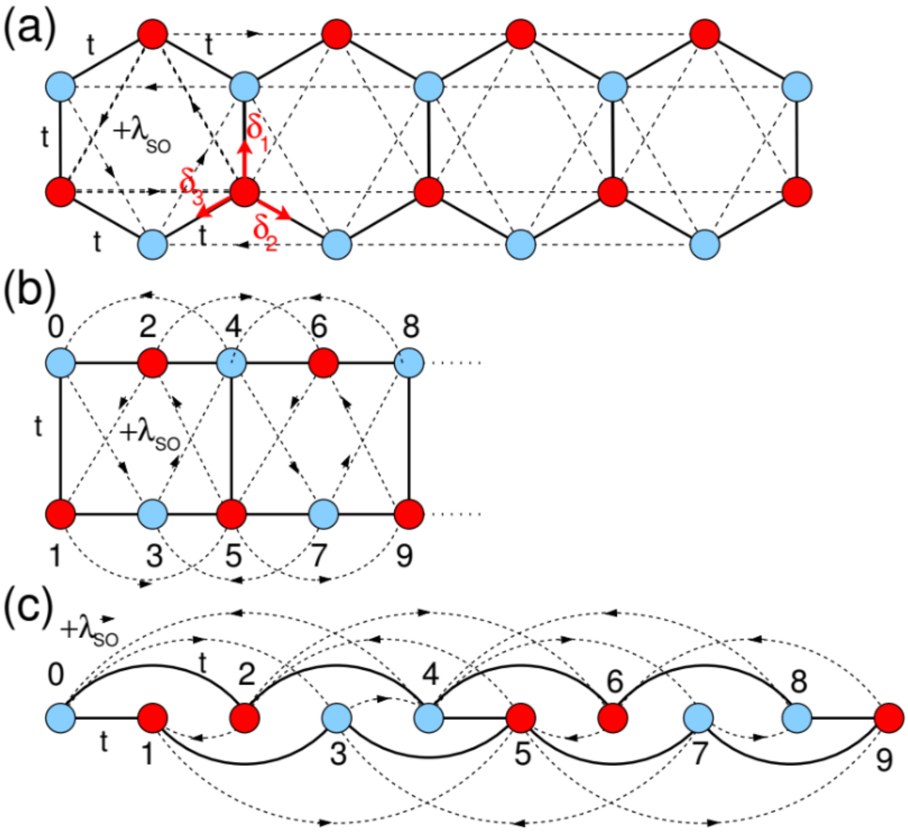

Figure 4.1: Kane-Mele-Hubbard ladders in (a) hexagonal chain and topologically equivalent forms of (b) stair and (c) linear chain, this last one proper to the DMRG algorithm.

In this one-dimensional configuration, we have to rewrite the spin-orbit term from Equation (2.5) as follows in order to implement it in the algorithm:

$$
\begin{aligned}
H_{\mathrm{SO}} &= i\lambda_{SO} \sum_{\langle\langle \mathbf{i},\mathbf{k}\rangle\rangle, s} c^{\dagger}_{\mathbf{i},s} (\hat{e}_{\mathbf{i},\mathbf{k}} \cdot \sigma)_{s,s'} c_{\mathbf{k},s'} \\
&= \pm i\lambda_{SO} \sum_{\langle\langle \mathbf{i},\mathbf{k}\rangle\rangle} (c^{\dagger}_{\mathbf{i},\uparrow} c^{\dagger}_{\mathbf{i},\downarrow}) \begin{pmatrix} 1 & 0 \\ 0 & -1 \end{pmatrix} \begin{pmatrix} c_{\mathbf{k},\uparrow} \\ c_{\mathbf{k},\downarrow} \end{pmatrix} \\
&= \pm i\lambda_{SO} \sum_{\langle\langle \mathbf{i},\mathbf{k}\rangle\rangle} (c^{\dagger}_{\mathbf{i},\uparrow} c_{\mathbf{k},\uparrow} - c^{\dagger}_{\mathbf{i},\downarrow} c_{\mathbf{k},\downarrow})\,.
\end{aligned}
\tag{4.1}
$$

Here, the change of **i** for **k** produces the Hermitian conjugate. This way, the phase sign depends on the geometry, as indicated in figure 4.1, as well as on the spin (opposite spins will have opposite phase signs).

Therefore, the Hamiltonian with all its terms for the Kane-Mele-Hubbard ladders, adequate for the DMRG calculations, can be written as

$$H_{\text{KMH}} = -t \sum_{\langle \mathbf{i},\mathbf{j} \rangle, s} c^{\dagger}_{\mathbf{i},s} c_{\mathbf{j},s} \pm i\lambda_{SO} \sum_{\langle\langle \mathbf{i},\mathbf{k} \rangle\rangle} (c^{\dagger}_{\mathbf{i},\uparrow} c_{\mathbf{k},\uparrow} - c^{\dagger}_{\mathbf{i},\downarrow} c_{\mathbf{k},\downarrow}) + U \sum_{\mathbf{i},s} \hat{n}_{\mathbf{i},\uparrow} \hat{n}_{\mathbf{i},\downarrow} \,. \tag{4.2}$$

4.2 Ground state energy finite size scaling

In Figure 4.2, we present the scaling of the ground state energy with the system size N. Evaluating this tendency, we can better understand how a system at the thermodynamic limit would behave.

Although we are now using a one-dimensional representation of the ladders, we cannot forget they started out as a honeycomb chain. Therefore, in order to study only systems consisting of full hexagons, the possible system's sizes are restricted to

$$N = 4n + 2 \,, \tag{4.3}$$

where $n = 1, 2...$ counts the number of hexagons.

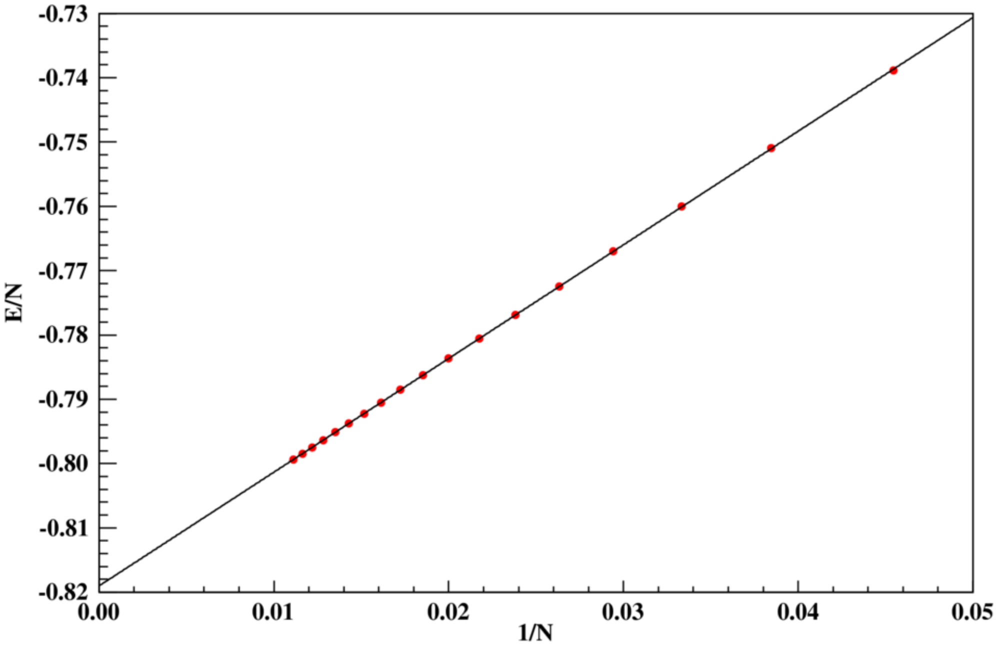

Figure 4.2: Finite-size scaling of the energy of the ground state, using chains of 22 to 90 sites, and parameters $t = 1$, $\lambda_{SO} = 0.5$, $U = 5$.

In Figure 4.2, we can clearly see a pattern of a straight line for the normalized ground state energy being formed. Adjusting the line via the method of least squares yields, in units of t, a value of -0.81901 ± 0.00003 for the energy of an infinite system.

Analyzing the ground-state energy for different parameters, we can better understand their effects in the system. In Figures 4.3 to 4.6, we can see the influence of U and λ_{SO} in the energy as the system size scales.

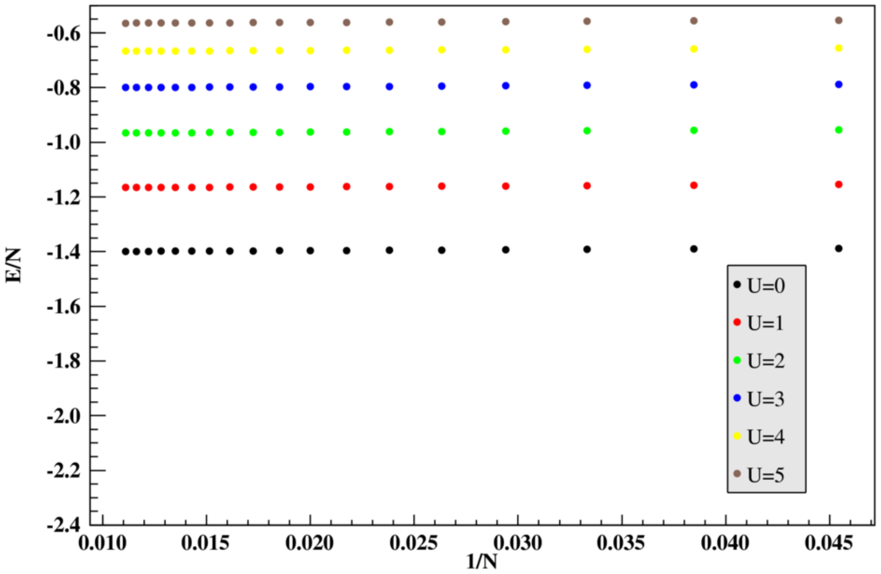

Figure 4.3: Finite-size scaling for the ground state energy with $t = 1$, $\lambda_{SO} = 0$ and varying U.

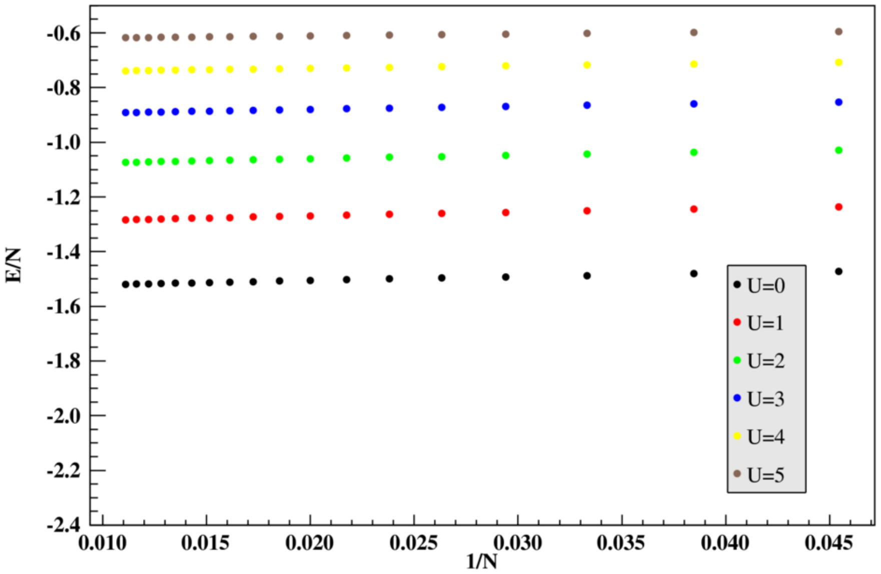

Figure 4.4: Finite-size scaling for the ground state energy with $t = 1$, $\lambda_{SO} = 0.25$ and varying U.

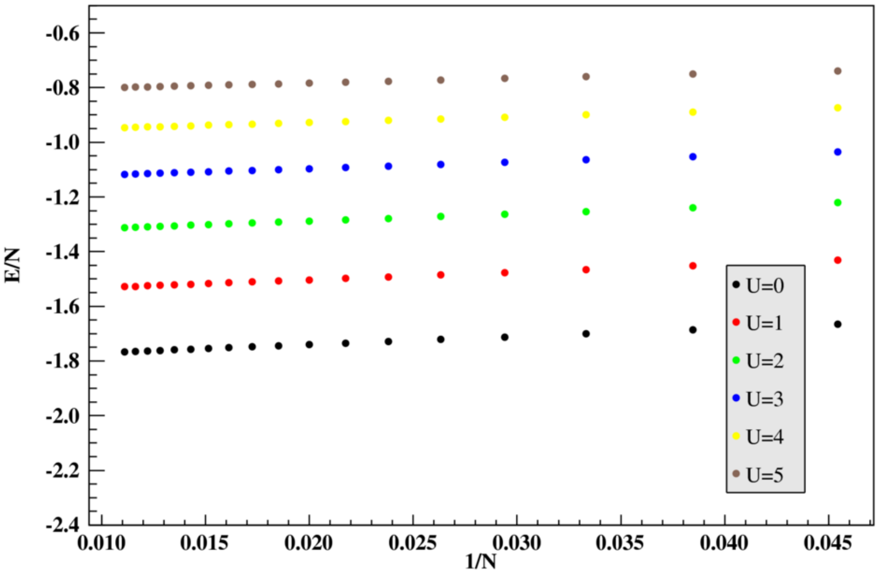

Figure 4.5: Finite-size scaling for the ground state energy with $t = 1$, $\lambda_{SO} = 0.5$ and varying U.

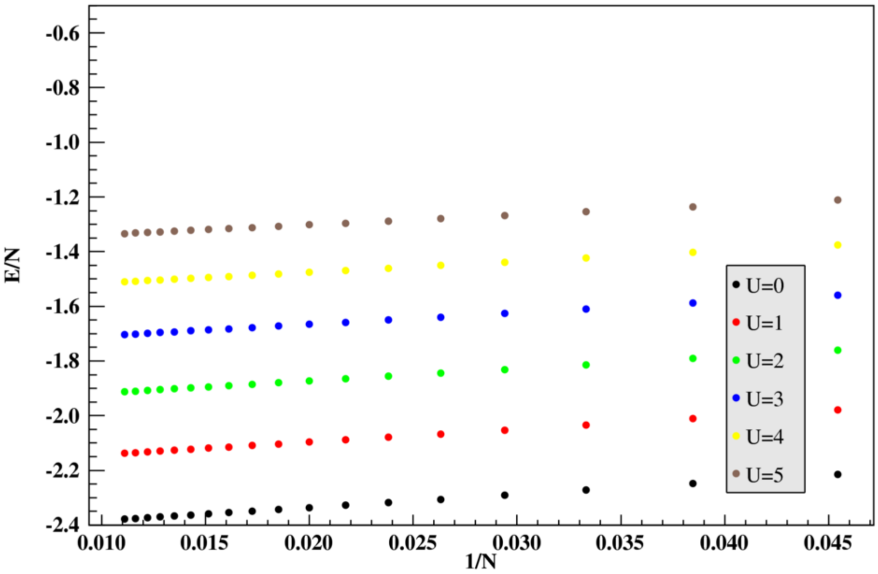

Figure 4.6: Finite-size scaling for the ground state energy with $t = 1$, $\lambda_{SO} = 1$ and varying U.

Figures 4.3 to 4.6 show us the behavior of the ground state energy as λ_{SO} and U change. For a given value of λ_{SO} and U the points tend to form a straight line as seen in Figure 4.2. By taking the same finite-size extrapolation and applying it to Figures 4.3 to 4.6, we can plot the ground state energies in the thermodynamic limit as a function of U and λ_{SO}, as shown in Figure 4.7.

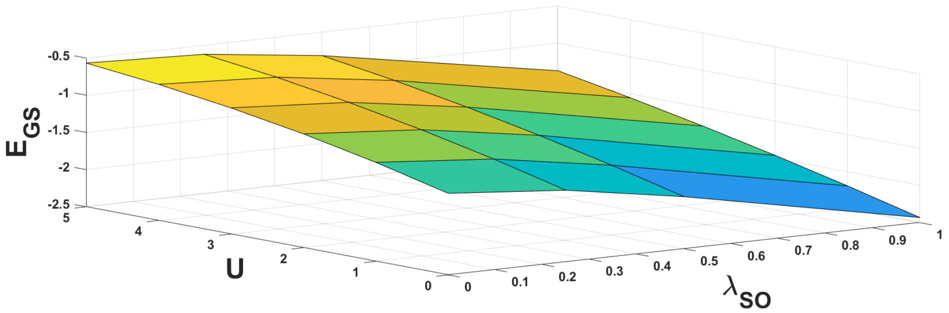

Figure 4.7: Contour plot of the ground state energy extrapolated to the thermodynamic limit as a function of λ_{SO} and U.

We can see in Figure 4.7 how λ_{SO} and U have competing effects in the ground state energy of the thermodynamic limit. While larger values of U yield higher energies, increases in λ_{SO} will diminish the energy.

4.3 Spin polarization

As stated before, topological insulators are insulators in the bulk, but present conducting edge states. In a QSHI, these states are polarized, meaning opposite spins are conducted in opposite directions in each edge of the system. But how does this property translates to the Kane-Mele-Hubbard ladders? We wanted to check if edge polarization remained present in this quasi-1D setting.

To do so, we measured the occupancy of electrons with each spin in all sites of the chain once the system reached the ground state. Then, we calculated the polarization on each site as the difference between the occupancy of spin up and spin down states, with results shown in Figures 4.9 and 4.10. We used varying values of λ and U in order to observe the behaviour of the polarization as a way to characterize the phase transition.

To aid the understanding of the polarization plots in Figures 4.9 and 4.10, Figure 4.8 specifies the numbering scheme adopted for the sites in the chain, as well as the color code used to represent the 4 types of sites:

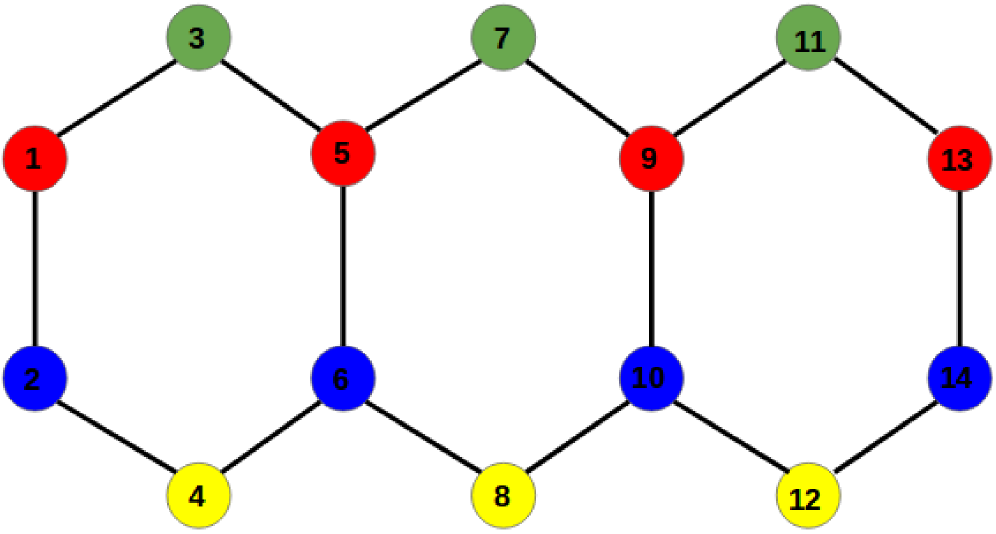

Figure 4.8: Color code for the 4 different types of sites in the chain, along with the numbering used for the sites.

In Figure 4.8, the numbering order was chosen to follow the linear chain configuration presented in Figure 4.1(c).

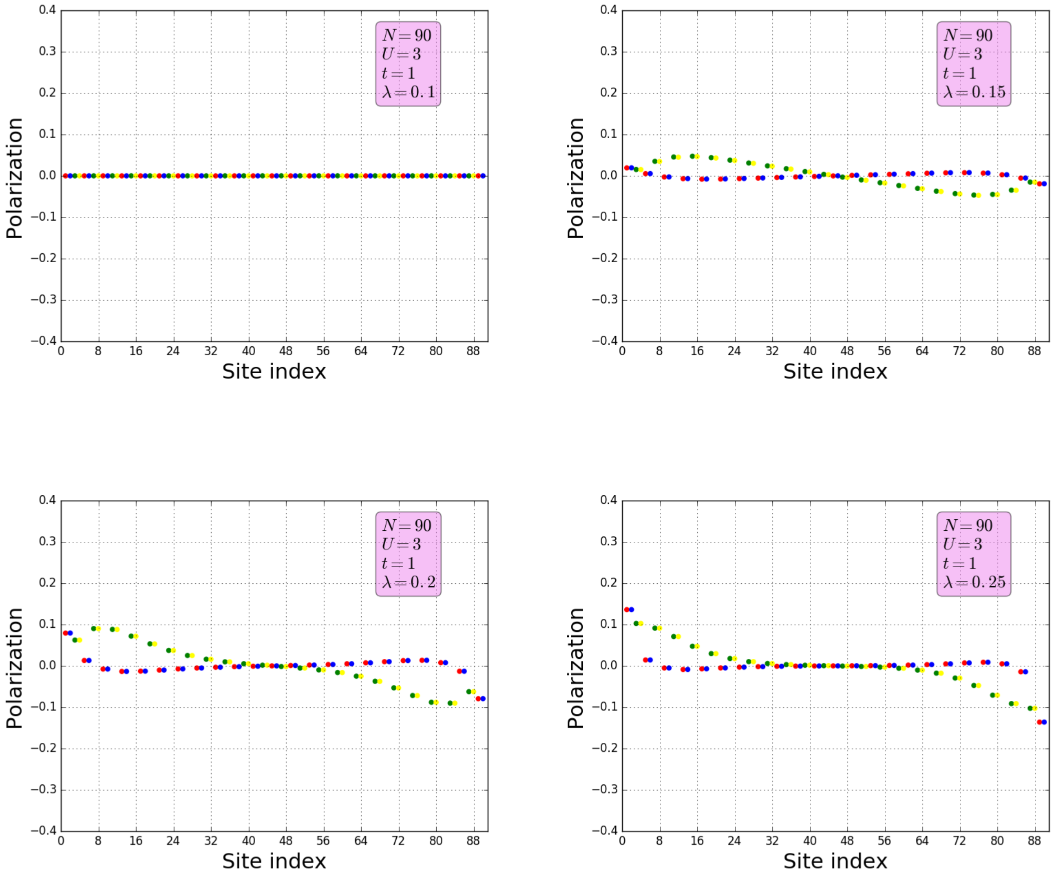

Figure 4.9: Spin polarization in all the 90 sites of the chain as λ increases.

The results in Figure 4.9 show that an increase in λ while the other parameters remain the same will naturally cause the appearance of spin-polarized states in the system. Moreover, the larger the value of λ, the more localized in the edges these states become. We attribute this to the topological phase transition taking place in the system.

Now, we can check how the polarized states depend on U. Analyzing the phase diagram for the two-dimensional Kane-Mele-Hubbard model in Figure 2.6, we see that starting from a Quantum Spin Hall phase, an increase in U leads to the Mott insulator phase, where edge states are not present. The question that arises from this is if such a behavior happens in the ladders as well. Looking at Figure 4.10, it seems so.

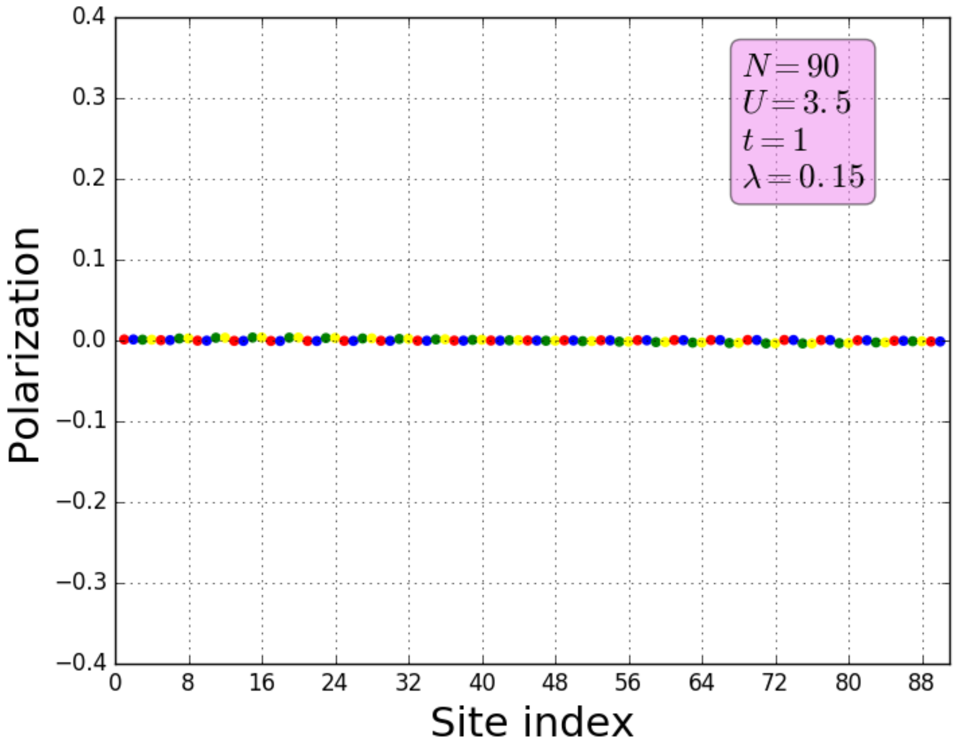

Figure 4.10: Spin polarization in the chain. The increase in U caused the disappearance of polarized states.

Figure 4.10 shows us that, as we would expected based on the two-dimensional case, spin polarization also disappears in the ladders if the value of U is increased when compared to the plots in Figure 4.9.

4.4 Entanglement entropy

Motivated by recent papers showing the correlation between entanglement entropy and topology in condensed matter [32] [33] [34], we decided to analyze how the entanglement entropy of the Kane-Mele-Hubbard ladders behaves as the phase transition takes place.

After taking the system to the ground state, we divided the system in half and calculated the entanglement entropy between the two partitions, as explained in Section 3.5.2. Figure 4.11 shows the behavior of the entanglement entropy of a system of fixed size $N = 90$ as the spin-orbit coupling changes.

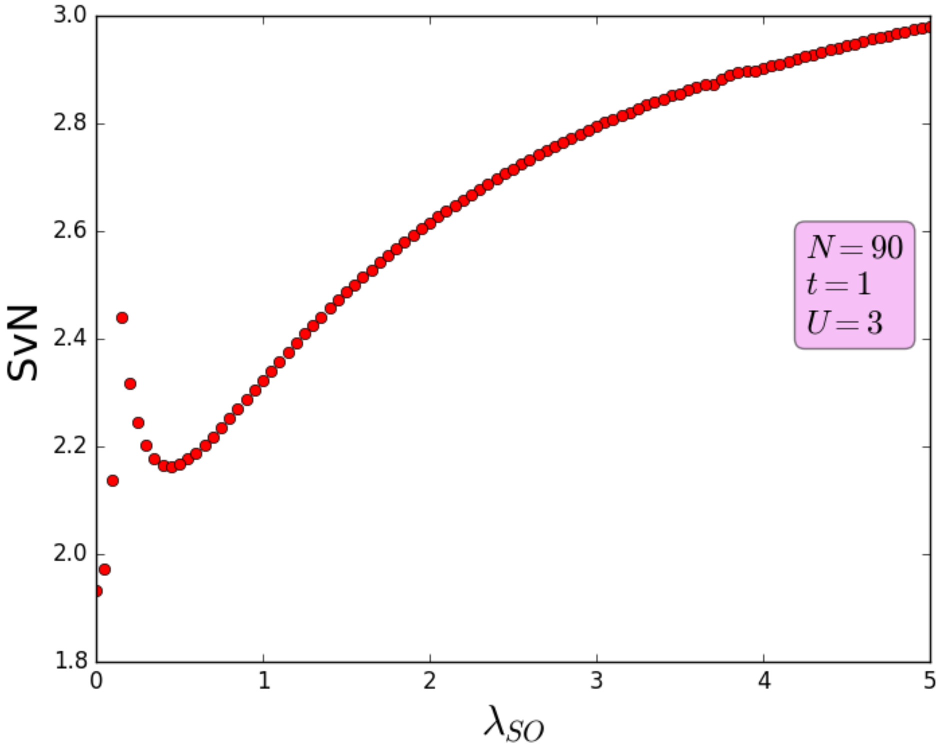

Figure 4.11: Entanglement entropy between the halves of the system as a function of λ.

The sudden increase in the entropy in Figure 4.11 happens in the same parameter region where the edge states appear on the system, as indicated by the polarization plots in Figure 4.9. This suggests that the entanglement entropy can be used as a way to identify the topological phase transition. To better investigate this idea, we decided to zoom into the region of the phase transition and check the influence of different values of U in the entropy as well, as seen in Figure 4.12.

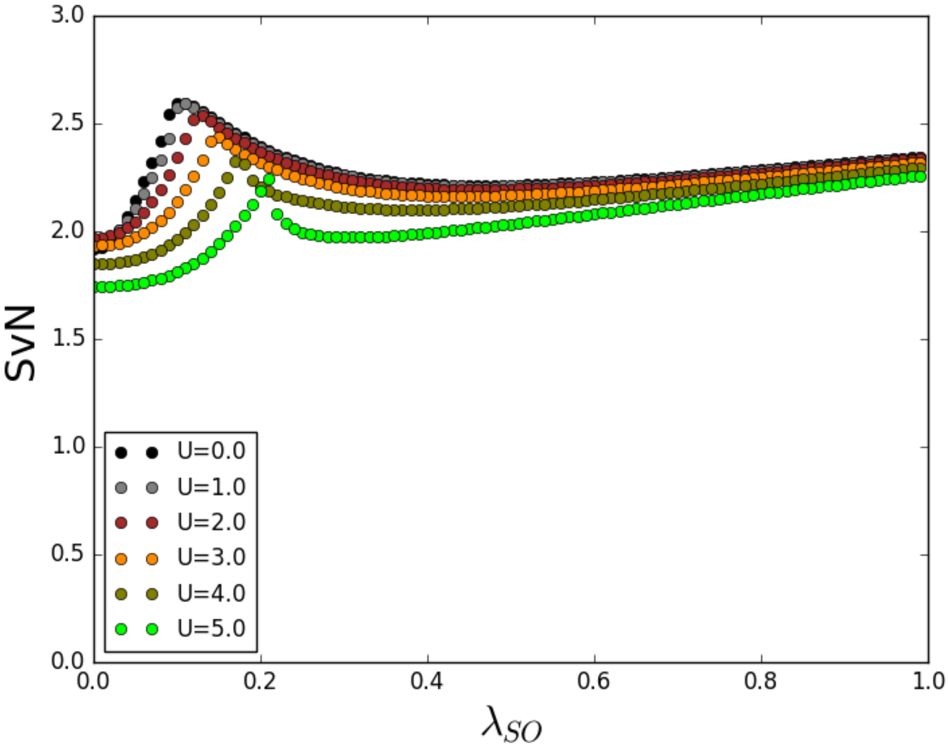

Figure 4.12: Zoom into the entanglement entropy (in the region of the phase transition), as a function of λ and for different values of U, for $N = 90$ sites.

It is noticeable how the sudden increase in entropy in Figure 4.12 is present for all values of U observed. Moreover, the larger is the value of U, the larger is the value of λ where the jump takes place. This can be understood as the phase transition between Mott insulator and topological insulator being governed by the values of these parameters: if U is large, the system will need a larger λ in order to go through the phase transition from Mott insulator to topological insulator.

In Ref. [34], the authors employed a DMRG algorithm and, among other things, computed the entanglement entropy of some 1D and quasi-1D quantum systems with topologically non-trivial phases. Notably, their results concerning the spin-1 bilinear-biquadractic model and the spin-1 Heisenberg tube model, respectively shown in Figures 4.14 and 4.15, present the same pattern of a sudden increase in the entanglement entropy in the region of the topological phase transition.

The spin-1 bilinear-biquadractic model is considered in a one-dimensional chain and can be represented by the following Hamiltonian

$$H_{blbq} = J \sum_{\langle i,j \rangle} [\cos(\theta) S_i S_j + \sin(\theta)(S_i S_j)^2] \,, \tag{4.4}$$

where J defines the energy scale and θ is a tunable parameter. It presents a topological phase transition at $\theta = -\pi/4$, going from a trivial gapped phase to a Haldane phase.

The three-leg spin-1 tube model is a quasi-1D model represented by the Hamiltonian

$$H_{tube} = J_L \sum_{i,a=[1,2,3]} S_{i,a} S_{i+1,a} + J_R \sum_i (S_{i,1} S_{i,2} + S_{i,2} S_{i,3} + \alpha S_{i,1} S_{i,3}) \,, \tag{4.5}$$

where J_L, J_R and α are coupling parameters as represented in Figure 4.13. For $J_L = 0.1$ and $J_R = 1$, the model is in the Haldane phase for $0 < \alpha < 0.57$ and in a trivial phase for $0.57 < \alpha < 1.5$. Thus, at $\alpha = 0.57$, a topological phase transition takes place.

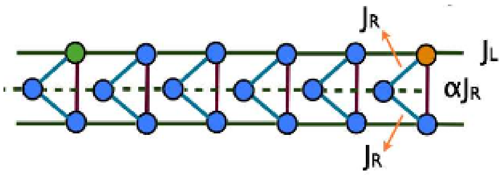

Figure 4.13: Figure from [34]. The three-leg spin tube model.

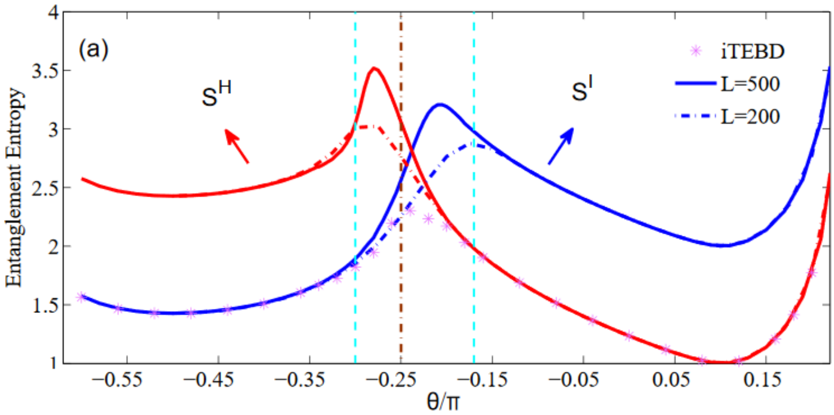

Figure 4.14: Figure from [34]. Entanglement entropy in the 1D bilinear-biquadractic model as a function of its tunable parameter θ. S^H (S^I) represents the system with half-integer (integer) spin representation on the ends of the chain. The dashed and full lines represent different sizes $L = 200, 500$ of the chain. All entanglement entropy curves present a sudden increase in the region of the topological phase transition, in the proximity of the vertical red dashed line.

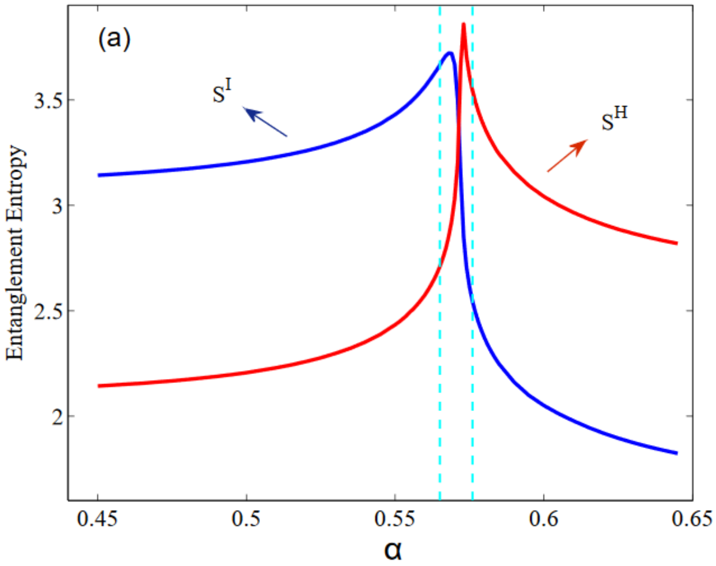

Figure 4.15: Figure from [34]. Entanglement entropy in the quasi-1D three-leg spin tube model as a function of its tunable parameter α. S^H (S^I) represents the system with half-integer (integer) spin representation on the ends of the chain. Both curves present a sudden increase in the region of the topological phase transition.

In Figures 4.14 and 4.15, the curves S^I and S^H represent the entanglement entropy for integer and half-integer spin representations on the boundary bonds, as defined in Ref. [34], while parameters α and θ are present in the Hamiltonians of their respective systems and govern their phase diagrams. The takeaway we want to highlight from these plots is that in the region of the topological phase transition, the entanglement entropy of these systems also presents the behavior we observed in the Kane-Mele-Hubbard ladders shown in Figures 4.11 and 4.12.

Chapter 5

Conclusions

In this work, we applied the tensor network formalism to study Kane-Mele-Hubbard ladders. Our goal is to better understand how the topological phase stemming from the Kane-Mele model behaves considering the addition of electronic interactions and the change in dimensionality.

We performed DMRG calculations in the half-filled honeycomb ladders to obtain the ground state energy of the system and calculated physical properties such as spin polarization and entanglement entropy. The calculations were carried out using the MPS formulation of DMRG, as explained in Chapter 3.

We managed to find linear relations between the size of the system and its ground state energy, leading us to extrapolate what would be the ground state energy in the thermodynamic limit. In Figure 4.7, we presented a plot showing the competing effects of the spin-orbit coupling and the on-site electron interactions on the ground state energy.

We also observed the appearance and disappearance of polarized edge states in the system, a phenomenon closely related to the values of λ and U. This shows the quasi-1D ladders follow the same behavior at criticality as the one from the phase diagram for the 2D Kane-Mele-Hubbard model in Figure 2.6. The region of the phase transition between Mott insulator and topological insulator is governed by these two parameters:

strong enough U will lead to a Mott insulator, while strong enough λ will lead to a topological insulator.

Finally, we were able to analyze the entanglement entropy between the two parts of the system as an indicator of the phase transition. As shown in Figure 4.11, we found a sudden jump in the entropy in the region of λ where the spin-polarized states appear. Looking closer, in Figure 4.12 we see that larger values of U cause this jump to occur with larger values of λ as well, thus matching the expectation on how these parameters govern the phase transition.

This pattern of the entanglement entropy curves is particularly relevant, as it matches the general behavior shown in Figures 4.14 and 4.15 from Ref. [34], where spin-1 1D and quasi-1D models with topological transitions were studied. This suggests the entanglement entropy can be a useful tool in investigations of other quasi-1D systems, working as a potential evidence of topological phase transitions.

Therefore, future developments based on this work can delve into this property of the entanglement entropy, and try to answer questions such as: what happens to the entanglement entropy between different partitions of the system (such as between edges and bulk) in the region of the topological phase transition? In what other quasi-1D models the entanglement entropy presents this same pattern? Can this behavior be observed in 2D systems as well? These are all important questions that might expand our understanding of topological phases of matter.

Bibliography

[1] Knig, M., Buhmann, H., W. Molenkamp, L., Hughes, T., Liu, C., Qi, X. and Zhang, S. (2008). The Quantum Spin Hall Effect: Theory and Experiment. Journal of the Physical Society of Japan, 77(3), p.031007.

[2] Zhang, H., Liu, C., Qi, X., Dai, X., Fang, Z. and Zhang, S. (2009). Topological insulators in Bi2Se3, Bi2Te3 and Sb2Te3 with a single Dirac cone on the surface. Nature Physics, 5(6), pp.438-442.

[3] Meng, Z., Lang, T., Wessel, S., Assaad, F. and Muramatsu, A. (2010). Quantum spin liquid emerging in two-dimensional correlated Dirac fermions. Nature, 464(7290), pp.847-851.

[4] Fiete, G., Chua, V., Kargarian, M., Lundgren, R., Regg, A., Wen, J. and Zyuzin, V. (2012). Topological insulators and quantum spin liquids. Physica E: Low-dimensional Systems and Nanostructures, 44(5), pp.845-859.

[5] Raghu, S., Qi, X., Honerkamp, C. and Zhang, S. (2008). Topological Mott Insulators. Physical Review Letters, 100(15).

[6] Dzero, M., Sun, K., Galitski, V. and Coleman, P. (2010). Topological Kondo Insulators. Physical Review Letters, 104(10).

[7] Hohenadler, M., Lang, T. and Assaad, F. (2011). Correlation Effects in Quantum Spin-Hall Insulators: A Quantum Monte Carlo Study. Physical Review Letters, 106(10).

[8] Wen, J., Kargarian, M., Vaezi, A. and Fiete, G. (2011). Doping the Kane-Mele-Hubbard model: A slave-boson approach. Physical Review B, 84(23).

[9] Itensor.org. (2019). ITensor - Intelligent Tensor Library (version 2.1.1). [online] Available at: http://itensor.org [Accessed 16 Jun. 2019].

[10] Kane, C. and Mele, E. (2005). Z2 Topological Order and the Quantum Spin Hall Effect. Physical Review Letters, 95(14).

[11] M. Hohenadler, F. Parisen Toldin, I. F. Herbut, F. F. Assaad. Phase diagram of the Kane-Mele-Coulomb model. *Phys. Rev. B* 90, 085146 (2014)

[12] Schollwöck, U. (2005). The density-matrix renormalization group. Reviews of Modern Physics, 77(1), pp.259-315.

[13] McCulloch, I. (2007). From density-matrix renormalization group to matrix product states. Journal of Statistical Mechanics: Theory and Experiment, 2007(10), pp.P10014-P10014.

[14] Schollwöck, U. (2011). The density-matrix renormalization group in the age of matrix product states. Annals of Physics, 326(1), pp.96-192.

[15] NobelPrize.org. (2019). The Nobel Prize in Physics 2016. [online] Available at: https://www.nobelprize.org/prizes/physics/2016/summary/ [Accessed 16 Jun. 2019].

[16] Klitzing, K., Dorda, G. and Pepper, M. (1980). New Method for High-Accuracy Determination of the Fine-Structure Constant Based on Quantized Hall Resistance. Physical Review Letters, 45(6), pp.494-497.

[17] S.Q. Shen. *Topological Insulators: Dirac Equation in Condensed Matter*. Springer Series in Solid-State Sciences. Springer-Verlag Berlin Heidelberg, 2012.

[18] Kane, C. and Mele, E. (2005). Quantum Spin Hall Effect in Graphene. Physical Review Letters, 95(22).

[19] Bernevig, B., Hughes, T. and Zhang, S. (2006). Quantum Spin Hall Effect and Topological Phase Transition in HgTe Quantum Wells. Science, 314(5806), pp.1757-1761.

[20] Konig, M., Wiedmann, S., Brune, C., Roth, A., Buhmann, H., Molenkamp, L., Qi, X. and Zhang, S. (2007). Quantum Spin Hall Insulator State in HgTe Quantum Wells. Science, 318(5851), pp.766-770.

[21] White, S. (1992). Density matrix formulation for quantum renormalization groups. Physical Review Letters, 69(19), pp.2863-2866.

[22] Itensor.org. (2019). ITensor - Intelligent Tensor Library. [online] Available at: http://www.itensor.org/docs.cgi?vers=cppv2&page=tutorials/cost [Accessed 17 Jun. 2019].

[23] M. Franz and L. Molenkamp. *Topological Insulators.* Contemporary Concepts of Condensed Matter Science. Elsevier Science, 2013.

[24] Thouless, D., Kohmoto, M., Nightingale, M. and den Nijs, M. (1982). Quantized Hall Conductance in a Two-Dimensional Periodic Potential. Physical Review Letters, 49(6), pp.405-408.

[25] Haldane, F. (1988). Model for a Quantum Hall Effect without Landau Levels: Condensed-Matter Realization of the "Parity Anomaly." Physical Review Letters, 61(18), pp.2015-2018.

[26] Fmt.if.usp.br. (2019). PGF5110 - Física do Estado Sólido I. [online] Available at: http://www.fmt.if.usp.br/~luisdias/Teaching/PosGrad/EstadoSolido2018/ [Accessed 17 Jun. 2019].

[27] Avella, Adolfo. and Mancini, Ferdinando. *Strongly Correlated Systems: Numerical Methods*. Springer Series in Solid-State Sciences. Springer-Verlag Berlin Heidelberg, 2013.

[28] Fmt.if.usp.br. (2019). Mini-Course: Tensor Networks and Applications - April 16-20 — Prof. Gabriel Teixeira Landi. [online] Available at: http://www.fmt.if.usp.br/~gtlandi/mini-course-tensor-networks.html [Accessed 17 Jun. 2019].

[29] Itensor.org. (2019). ITensor - Intelligent Tensor Library. [online] Available at: https://itensor.org/docs.cgi?page=classes/autompo&vers=cppv2 [Accessed 10 Jul. 2019].

[30] Davidson, E. (1975). The iterative calculation of a few of the lowest eigenvalues and corresponding eigenvectors of large real-symmetric matrices. Journal of Computational Physics, 17(1), pp.87-94.

[31] Lanczos, C. (1950). An iteration method for the solution of the eigenvalue problem of linear differential and integral operators. Journal of Research of the National Bureau of Standards, 45(4), p.255.

[32] Jiang, H., Wang, Z. and Balents, L. (2012). Identifying topological order by entanglement entropy. Nature Physics, 8(12), pp.902-905.

[33] Kitaev, A. and Preskill, J. (2006). Topological Entanglement Entropy. Physical Review Letters, 96(11).

[34] Li, W., Weichselbaum, A. and Delft, J. (2013). Identifying symmetry-protected topological order by entanglement entropy. Physical Review B, 88(24).

Appendix A

Kane-Mele model tight-binding Hamiltonian

In this appendix, in order to elucidate how the simplified Kane-Mele model presented in Equation (2.4) can be studied analytically, we present its tight-binding formulation for the first neighbor's hopping terms. The generalization for second neighbor's spin-orbit interactions can be conducted by combining two levels of the same orbital wave functions, but with opposite spins having different geometric signs as explained in Section 2.3.

Let us consider an hexagonal lattice with sides of length a, as Figure A.1 shows. We can write the vectors of the basis as

$$
\begin{aligned}
\vec{\delta}_B &= a\hat{y}\,, \\
\vec{\delta}_C &= \frac{\sqrt{3}a}{2}\hat{x} + \frac{a}{2}(-\hat{y})\,, \\
\vec{\delta}_D &= \frac{\sqrt{3}a}{2}\hat{x} + \frac{3a}{2}\hat{y}\,, \\
\vec{\delta} &= \frac{\sqrt{3}a}{2}\hat{x} + \frac{a}{2}\hat{y}\,.
\end{aligned}
$$

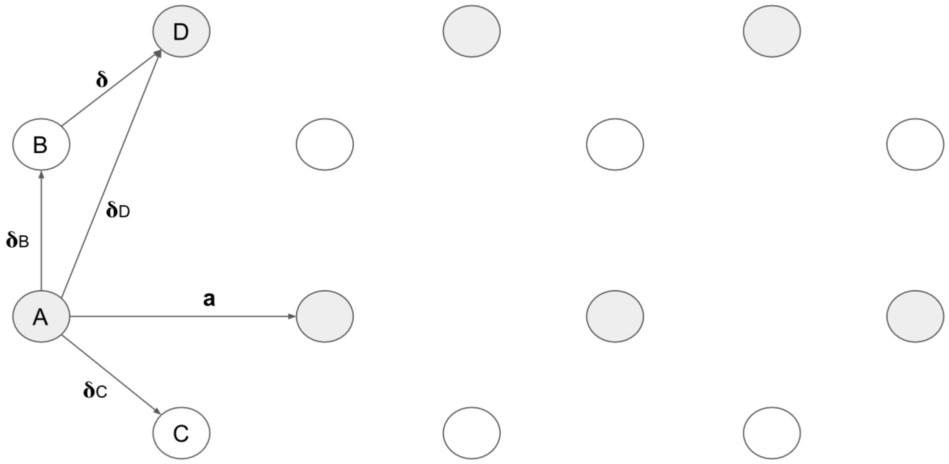

Figure A.1: Hexagonal chain with vector basis.

Given Bloch's Theorem, we can write the Bloch functions for sites A, B, C and D

$$\begin{aligned}
\Psi^{(A)}_{\vec{q}}(\vec{r}) &= \sum_{\vec{R}'} e^{i\vec{q}\cdot\vec{R}'}\Phi_A(\vec{r}-\vec{R}')\,,\\
\Psi^{(B)}_{\vec{q}}(\vec{r}) &= \sum_{\vec{R}'} e^{i\vec{q}\cdot\vec{R}'}\Phi_B(\vec{r}-\vec{\delta}_B-\vec{R}')\,,\\
\Psi^{(C)}_{\vec{q}}(\vec{r}) &= \sum_{\vec{R}'} e^{i\vec{q}\cdot\vec{R}'}\Phi_C(\vec{r}-\vec{\delta}_C-\vec{R}')\,,\\
\Psi^{(D)}_{\vec{q}}(\vec{r}) &= \sum_{\vec{R}'} e^{i\vec{q}\cdot\vec{R}'}\Phi_D(\vec{r}-\vec{\delta}_D-\vec{R}')\,,
\end{aligned} \tag{A.1}$$

such that the wave function will be a linear combination of the four Bloch functions

$$\Psi_{\vec{q}}(\vec{r}) = a_{\vec{q}}\Psi^{(A)}_{\vec{q}}(\vec{r}) + b_{\vec{q}}\Psi^{(B)}_{\vec{q}}(\vec{r}) + c_{\vec{q}}\Psi^{(C)}_{\vec{q}}(\vec{r}) + d_{\vec{q}}\Psi^{(D)}_{\vec{q}}(\vec{r})\,. \tag{A.2}$$

We can then consider the Hamiltonian composed by two parts

$$H = H_{at} + \Delta V\,, \tag{A.3}$$

where

$$H_{at}\Psi_{\vec{q}}(\vec{r}) = \epsilon_0 \Psi_{\vec{q}}(\vec{r})\,, \tag{A.4}$$

and write it as a 4x4 matrix

$$H_{\vec{q}} = \begin{pmatrix} H_{\vec{q}}^{AA} & H_{\vec{q}}^{AB} & H_{\vec{q}}^{AC} & H_{\vec{q}}^{AD} \\ H_{\vec{q}}^{BA} & H_{\vec{q}}^{BB} & H_{\vec{q}}^{BC} & H_{\vec{q}}^{BD} \\ H_{\vec{q}}^{CA} & H_{\vec{q}}^{CB} & H_{\vec{q}}^{CC} & H_{\vec{q}}^{CD} \\ H_{\vec{q}}^{DA} & H_{\vec{q}}^{DB} & H_{\vec{q}}^{DC} & H_{\vec{q}}^{DD} \end{pmatrix},$$

in which each element $H_{\vec{q}}^{i,j}$ is given by

$$H_{\vec{q}}^{i,j} = \int \Psi_{\vec{q}}^{(i)}(\vec{r})^* \; H \; \Psi_{\vec{q}}^{(j)}(\vec{r}) \; d^2\vec{r}\,. \tag{A.5}$$

As we are only considering first-neighbor interactions, we have

$$\boxed{H_{\vec{q}}^{AD} = H_{\vec{q}}^{DA} = H_{\vec{q}}^{BC} = H_{\vec{q}}^{CB} = H_{\vec{q}}^{CD} = H_{\vec{q}}^{DC} = 0}\,. \tag{A.6}$$

Now we have to check the other cases. For AA, we will have only one site of type A being considered:

$$\begin{aligned} H_{\vec{q}}^{AA} = & \underbrace{\sum_{\vec{R}'} e^{i\vec{q}\cdot(\vec{R}'-\vec{R}')} \int \Phi_A^*(\vec{r}-\vec{R}')\epsilon_0 \Phi_A(\vec{r}-\vec{R}') d^2\vec{r}}_{\epsilon_0 S_{\vec{q}}^{AA}} \\ & + \underbrace{\sum_{\vec{R}'} e^{i\vec{q}\cdot(\vec{R}'-\vec{R}')} \int \Phi_A^*(\vec{r}-\vec{R}')\Delta V \Phi_A(\vec{r}-\vec{R}') d^2\vec{r}}_{t_{\vec{q}}^{AA}}, \end{aligned} \tag{A.7}$$

where

$$
\begin{aligned}
S_{\vec{q}}^{AA} &= N\,, \\
t_{\vec{q}}^{AA} &= \sum_{\vec{R}'} \underbrace{\int \Phi_A^*(\vec{r}-\vec{R}')\Delta V \Phi_A(\vec{r}-\vec{R}')d^2\vec{r}}_{\Delta\epsilon} = N t_{AA}\,.
\end{aligned}
$$

Therefore,

$$\boxed{H_{\vec{q}}^{AA} = N(\epsilon_0 + \Delta\epsilon)}\,, \tag{A.8}$$

and the same result is valid for cases BB, CC and DD. Now treating the case BA, where site A has one neighbor of type B in position $\vec{\delta}_B$:

$$
\begin{aligned}
S_{\vec{q}}^{BA} &= \sum_{\vec{R}',\vec{R}''} e^{i\vec{q}\cdot(\vec{R}'-\vec{R}'')} \int \Phi_B^*(\vec{r}-\vec{\delta}_B-\vec{R}'')\Phi_A(\vec{r}-\vec{R}')d^2\vec{r} \\
&= \sum_{\vec{R}'} \underbrace{\int \Phi_B^*(\vec{r}-\vec{\delta}_B-\vec{R}')\Phi_A(\vec{r}-\vec{R}')d^2\vec{r}}_{S_{BA}} \\
&= N S_{BA}\,,
\end{aligned}
$$

$$
\begin{aligned}
t_{\vec{q}}^{BA} &= \sum_{\vec{R}'} \underbrace{\int \Phi_B^*(\vec{r}-\vec{\delta}_B-\vec{R}')\Delta V \Phi_A(\vec{r}-\vec{R}')d^2\vec{r}}_{t_{BA}}\,, \\
&= N t_{BA}
\end{aligned}
$$

$$\boxed{H_{\vec{q}}^{BA} = N(\epsilon_0 S_{BA} + t_{BA}) = (H_{\vec{q}}^{AB})^*}\,. \tag{A.9}$$

Now, for the CA case, site A has two type C neighbors in positions $\vec{\delta}_C$ and $\vec{\delta}_C - \vec{a}$:

$$
\begin{aligned}
S_{\vec{q}}^{CA} &= \sum_{\vec{R}',\vec{R}''} e^{i\vec{q}\cdot(\vec{R}'-\vec{R}'')} \int \Phi_C^*(\vec{r}-\vec{\delta}_C-\vec{R}'')\Phi_A(\vec{r}-\vec{R}')d^2\vec{r} \\
&= \sum_{\vec{R}'} e^{i\vec{q}\cdot\vec{R}'} \Bigg(\int \Phi_C^*(\vec{r}-\vec{\delta}_C-\vec{R}')\Phi_A(\vec{r}-\vec{R}')e^{-i\vec{q}\cdot\vec{R}'}d^2\vec{r} \\
&+ \int \Phi_C^*(\vec{r}-\vec{\delta}_C+\vec{a}-\vec{R}')\Phi_A(\vec{r}-\vec{R}')e^{-i\vec{q}\cdot(\vec{R}'-\vec{a})}d^2\vec{r} \Bigg) \\
&= \sum_{\vec{R}'} \underbrace{\int \Phi_C^*(\vec{r}-\vec{\delta}_C-\vec{R}')\Phi_A(\vec{r}-\vec{R}')d^2\vec{r}}_{S_{CA}} \; (1+e^{-i\vec{q}\cdot\vec{a}}) \\
&= N S_{CA}(1+e^{-i\vec{q}\cdot\vec{a}})\,,
\end{aligned}
$$

$$
\begin{aligned}
t_{\vec{q}}^{CA} &= \sum_{\vec{R}'} e^{i\vec{q}\cdot\vec{R}'} \Bigg(\int \Phi_C^*(\vec{r}-\vec{\delta}_C-\vec{R}')\Delta V \Phi_A(\vec{r}-\vec{R}')e^{-i\vec{q}\cdot\vec{R}'}d^2\vec{r} \\
&+ \int \Phi_C^*(\vec{r}-\vec{\delta}_C+\vec{a}-\vec{R}')\Delta V \Phi_A(\vec{r}-\vec{R}')e^{-i\vec{q}\cdot(\vec{R}'-\vec{a})}d^2\vec{r} \Bigg) \\
&= \sum_{\vec{R}'} \underbrace{\int \Phi_C^*(\vec{r}-\vec{\delta}_C-\vec{R}')\Delta V \Phi_A(\vec{r}-\vec{R}')d^2\vec{r}}_{t_{CA}} \; (1+e^{-i\vec{q}\cdot\vec{a}}) \\
&= N t_{CA}(1+e^{-i\vec{q}\cdot\vec{a}})\,,
\end{aligned}
$$

$$
\boxed{H_{\vec{q}}^{CA} = N(1+e^{-i\vec{q}\cdot\vec{a}})(\epsilon_0 S_{CA} + t_{CA}) = (H_{\vec{q}}^{AC})^*}\,. \tag{A.10}
$$

Likewise, for BD, site B has two neighbors of type D in positions $\vec{\delta}$ and $\vec{\delta}-\vec{a}$:

$$
\begin{aligned}
S_{\vec{q}}^{BD} &= \sum_{\vec{R'},\vec{R''}} e^{i\vec{q}\cdot(\vec{R'}-\vec{R''})} \int \Phi_B^*(\vec{r}-\vec{\delta}-\vec{R''})\Phi_D(\vec{r}-\vec{R'})d^2\vec{r} \\
&= \sum_{\vec{R'}} e^{i\vec{q}\cdot\vec{R'}} \left(\int \Phi_B^*(\vec{r}-\vec{\delta}-\vec{R'})\Phi_D(\vec{r}-\vec{R'})e^{-i\vec{q}\cdot\vec{R'}}d^2\vec{r} \right. \\
&\left. + \int \Phi_B^*(\vec{r}-\vec{\delta}+\vec{a}-\vec{R'})\Phi_D(\vec{r}-\vec{R'})e^{-i\vec{q}\cdot(\vec{R'}-\vec{a})}d^2\vec{r} \right) \\
&= \sum_{\vec{R'}} \underbrace{\int \Phi_B^*(\vec{r}-\vec{\delta}-\vec{R'})\Phi_D(\vec{r}-\vec{R'})d^2\vec{r}}_{S_{BD}} \, (1+e^{-i\vec{q}\cdot\vec{a}}) \\
&= NS_{BD}(1+e^{-i\vec{q}\cdot\vec{a}}) \, ,
\end{aligned}
$$

$$
\begin{aligned}
t_{\vec{q}}^{BD} &= \sum_{\vec{R'}} e^{i\vec{q}\cdot\vec{R'}} \left(\int \Phi_B^*(\vec{r}-\vec{\delta}-\vec{R'})\Delta V \Phi_D(\vec{r}-\vec{R'})e^{-i\vec{q}\cdot\vec{R'}}d^2\vec{r} \right. \\
&\left. + \int \Phi_B^*(\vec{r}-\vec{\delta}+\vec{a}-\vec{R'})\Delta V \Phi_D(\vec{r}-\vec{R'})e^{-i\vec{q}\cdot(\vec{R'}-\vec{a})}d^2\vec{r} \right) \\
&= \sum_{\vec{R'}} \underbrace{\int \Phi_B^*(\vec{r}-\vec{\delta}-\vec{R'})\Delta V \Phi_D(\vec{r}-\vec{R'})d^2\vec{r}}_{t_{BD}} \, (1+e^{-i\vec{q}\cdot\vec{a}}) \\
&= Nt_{BD}(1+e^{-i\vec{q}\cdot\vec{a}}) \, ,
\end{aligned}
$$

$$
\boxed{H_{\vec{q}}^{BD} = N(1+e^{-i\vec{q}\cdot\vec{a}})(\epsilon_0 S_{BD} + t_{BD}) = (H_{\vec{q}}^{DB})^*} \, . \tag{A.11}
$$

Thus, the matrix form of the tight-binding Hamiltonian is given by

$$
\frac{H_{\vec{q}}}{N} = \begin{pmatrix}
\epsilon_0+\Delta\epsilon & \epsilon_0 S_{BA}^*+t_{BA}^* & (\epsilon_0 S_{CA}^*+t_{CA}^*)(1+e^{i\vec{q}\cdot\vec{a}}) & 0 \\
\epsilon_0 S_{BA}+t_{BA} & \epsilon_0+\Delta\epsilon & 0 & (\epsilon_0 S_{BD}^*+t_{BD}^*)(1+e^{i\vec{q}\cdot\vec{a}}) \\
(\epsilon_0 S_{CA}+t_{CA})(1+e^{-i\vec{q}\cdot\vec{a}}) & 0 & \epsilon_0+\Delta\epsilon & 0 \\
0 & (\epsilon_0 S_{BD}+t_{BD})(1+e^{-i\vec{q}\cdot\vec{a}}) & 0 & \epsilon_0+\Delta\epsilon
\end{pmatrix}
$$

Annex I

Best Poster Award at the Brazilian Physical Society Autumn Meeting

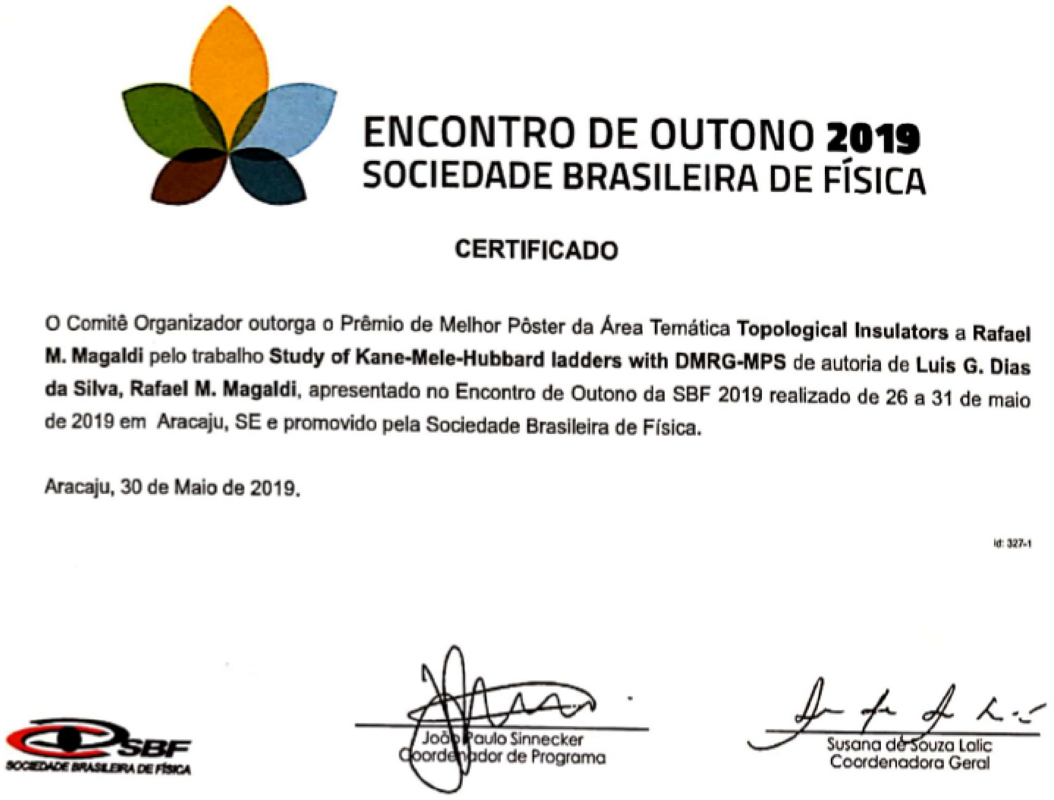

ENCONTRO DE OUTONO **2019**
SOCIEDADE BRASILEIRA DE FÍSICA

CERTIFICADO

O Comitê Organizador outorga o Prêmio de Melhor Pôster da Área Temática **Topological Insulators** a **Rafael M. Magaldi** pelo trabalho **Study of Kane-Mele-Hubbard ladders with DMRG-MPS** de autoria de **Luis G. Dias da Silva, Rafael M. Magaldi**, apresentado no Encontro de Outono da SBF 2019 realizado de 26 a 31 de maio de 2019 em Aracaju, SE e promovido pela Sociedade Brasileira de Física.

Aracaju, 30 de Maio de 2019.

id: 327-1

SBF
SOCIEDADE BRASILEIRA DE FÍSICA

João Paulo Sinnecker
Coordenador de Programa

Susana de Souza Lalic
Coordenadora Geral